NATIONAL ADVISORY COMMITTEE FOR AERONAUTICS

TECHNICAL NOTE 3611

ANALYSIS OF A SPIN AND RECOVERY FROM TIME HISTORIES OF ATTITUDES AND VELOCITIES AS DETERMINED FOR A DYNAMIC MODEL OF A CONTEMPORARY FIGHTER AIRPLANE IN THE FREE-SPINNING TUNNEL

By Stanley H. Scher

Langley Aeronautical Laboratory
Langley Field, Va.

Washington
April 1956

1K

NATIONAL ADVISORY COMMITTEE FOR AERONAUTICS

TECHNICAL NOTE 3611

ANALYSIS OF A SPIN AND RECOVERY FROM TIME HISTORIES OF ATTITUDES AND VELOCITIES AS DETERMINED FOR A DYNAMIC MODEL OF A CONTEMPORARY FIGHTER AIRPLANE IN THE FREE-SPINNING TUNNEL

By Stanley H. Scher

SUMMARY

In order to obtain a broader understanding of the factors which affect spin and recovery motions, a technique has been devised for determining time histories of the attitudes and velocities of free-spinning-tunnel models from film taken by two motion-picture cameras operating simultaneously. This paper presents the method devised and the results of an initial application of the method in which time histories of attitudes and velocities have been determined for one medium-attitude, moderately oscillatory, developed spin and the recovery therefrom for a model representative of a contemporary fighter airplane.

The time-history curves indicated that the oscillatory motion of the spin was not completely regular, inasmuch as the period and amplitude of any one cycle of the time histories were not exactly the same as those for the preceding and following cycles. After rudder reversal from with to against the spin, some increases occurred in the amplitude of the oscillations, particularly in the lateral attitude angles of sideslip and wing tilt. The recovery was completed about $1\frac{1}{2}$ turns after the rudder was reversed. One factor which appeared to have an important part in the attainment of the recovery from the spin in this investigation was a relatively high inward sideslip reached during the oscillations following rudder reversal. Analysis indicates that the high inward sideslip apparently caused a relatively large negative aerodynamic rolling moment which caused a large decrease in rolling velocity; as a result, there was a corresponding large decrease in the gyrodynamic pitching moment which had been holding the model in a nose-up spinning attitude.

INTRODUCTION

Many investigations have been made in the Langley 20-foot free-spinning tunnel in which airplane spin and recovery characteristics have been determined experimentally with dynamically scaled models. The results of a few such investigations are presented in references 1 to 5. From the results of the free-spinning-tunnel tests, it has been possible to evaluate some of the factors affecting spins and recoveries. However, with the advent of modern high-speed airplanes with design features such as extreme fuselage-heavy loadings, long nose lengths, and thin sweptback wings, the complexity of the spinning problem has been accentuated. As one means of obtaining a broader understanding of the factors affecting spins and recoveries, a technique has been devised for determining time histories of the attitudes and velocities of the models from film taken by two simultaneously operating motion-picture cameras. As an initial application of this technique, an investigation has been made to determine time histories of the attitudes and velocities during one spin and the recovery therefrom for a model representative of a contemporary fighter airplane.

In this paper are presented descriptions of the camera setups and associated equipment, the equations and methods used in determining the model attitudes and motions from the film, and time-history curves of the variables of the spin and recovery investigated. The attitudes and velocities are plotted with respect to airplane body axes, the earth, the relative wind, and the axis of the resultant rotary motion. The curves show the attitudes and velocities of the model for a continuous time period of about 19 seconds (full-scale time), of which the first 12.5 seconds or so represent about $3\frac{1}{4}$ turns of a developed spin and the remaining time represents a $1\frac{1}{2}$-turn recovery from the spin. Discussions of the nature of the spin and recovery obtained and of factors ostensibly affecting these motions are included.

SYMBOLS

The time-history plots are presented with respect to the airplane body system of axes and to space and wind attitude angles (fig. 1).

X,Y,Z airplane body axes

C_l rolling-moment coefficient, $\dfrac{L}{\frac{1}{2}\rho V_R{}^2 Sb}$

C_m pitching-moment coefficient, $\frac{M}{\frac{1}{2}\rho V_R^{2}Sb}$

C_n yawing-moment coefficient, $\frac{N}{\frac{1}{2}\rho V_R^{2}Sb}$

C_X longitudinal-force coefficient, $\frac{F_X}{\frac{1}{2}\rho V_R^{2}S}$

C_Y lateral-force coefficient, $\frac{F_Y}{\frac{1}{2}\rho V_R^{2}S}$

C_Z normal-force coefficient, $\frac{F_Z}{\frac{1}{2}\rho V_R^{2}S}$

L rolling moment, ft-lb

M pitching moment, ft-lb

N yawing moment, ft-lb

F_X longitudinal force, lb

F_Y lateral force, lb

F_Z normal force, lb

S wing area, sq ft

b wing span, ft

ρ air density, slugs/cu ft

u,v,w components of resultant linear velocity V_R along the X, Y, and Z body axes, respectively, positive in directions of positive X-, Y-, and Z-forces, ft/sec

V_R resultant linear velocity, ft/sec

p,q,r components of resultant angular velocity Ω about X, Y, and Z body axes, respectively, positive in directions of positive L-, M-, and N-moments, radians/sec

Ω resultant angular velocity (if axis of resultant rotation is vertical, $\Omega = \dot{\psi}_e$), radians/sec

μ airplane relative-density coefficient, $\frac{m}{\rho Sb}$

m mass of airplane, $\frac{\text{Weight}}{g}$, slugs

$\bar{c}$ mean aerodynamic chord, ft

$x/\bar{c}$ ratio of distance of center of gravity rearward of leading edge of mean aerodynamic chord to mean aerodynamic chord

$z/\bar{c}$ ratio of distance between center of gravity and X body axis to mean aerodynamic chord (positive when center of gravity is below X body axis)

I_X,I_Y,I_Z moments of inertia about X, Y, and Z body axes, respectively, slug-ft^2

I_{XZ} product of inertia about X and Z body axes, slug-ft^2

$\frac{I_X - I_Y}{mb^2}$ inertia yawing-moment parameter

$\frac{I_Y - I_Z}{mb^2}$ inertia rolling-moment parameter

$\frac{I_Z - I_X}{mb^2}$ inertia pitching-moment parameter

g acceleration due to gravity, taken as 32.17 ft/sec^2

θ_e projection in vertical plane of total angular deflection of X body axis from a reference position in horizontal plane, positive when sense of deflection is airplane nose upward from reference position, deg or radians as indicated (fig. 1(a))

ψ_e — projection in horizontal plane of total angular defelction of X body axis from reference position in horizontal plane, positive when clockwise as viewed vertically from above airplane, deg or radians as indicated (fig. 1(b))

ϕ_e — angular deflection in YZ body plane of Y body axis from horizontal plane, positive when clockwise as viewed from rear of airplane (if X body axis is vertical, ϕ_e is measured in horizontal plane from a reference line in this plane), deg or radians as indicated (fig. 1(c))

ϕ — angle between Y body axis and horizontal, positive for erect spins when airplane right wing is down and for inverted spins when airplane left wing is down, deg

α_1 — acute angle between X body axis and vertical, deg

α_3 — acute angle between Z body axis and horizontal, deg

α_1' — angle between X body axis and axis of resultant rotation,

$$\cos^{-1}\frac{p}{\Omega} \quad \text{or} \quad \sin^{-1}\frac{\sqrt{r^2 + q^2}}{\Omega}, \text{ deg}$$

α — angle of attack between relative wind V_R projected into XZ plane of symmetry and X body axis, positive when relative wind comes from below XY body plane, deg

β — angle of sideslip at center of gravity (angle between relative wind V_R and XZ plane of symmetry), positive when relative wind comes from right side of plane of symmetry, deg

τ_{VR} — angle of inclination of relative wind V_R from XY body plane, positive when inclined below XY body plane, $\sin^{-1}\frac{w}{V_R}$, deg

δ_{VR} — angle between relative wind V_R projected into XY body plane and X body axis, positive when V_R comes from right side of plane of symmetry, $\sin^{-1}\frac{v}{\sqrt{u^2 + v^2}}$, deg

τ_Ω angle of inclination of axis of resultant rotation from XY body plane, positive when inclined below XY body plane, $\sin^{-1} \frac{r}{\Omega}$, deg

δ_Ω angle between axis of resultant rotation projected into XY body plane and X body axis, positive when vector of axis of resultant rotation lies on right side of plane of symmetry, $\sin^{-1} \frac{q}{\sqrt{p^2 + q^2}}$, deg

t time, sec

σ acute angle between direction of resultant linear velocity and axis of resultant rotation, deg

V velocity of airplane center of gravity along axis of resultant rotation, $V_R \cos \sigma$, ft/sec

κ_Ω angle between axis of resultant rotation and vertical, deg

κ_{VR} angle between resultant linear velocity and vertical, deg

V_V vertical component of velocity of airplane center of gravity, ft/sec

P_H horizontal reference plane at eye level in tunnel, 23.48 feet above center of bottom-camera lens (fig. 19)

Q fixed reference point where a vertical line through the side camera stanchion and pivot point intersects P_H; Q is 10.95 feet from center of tunnel (fig. 19)

P_V vertical reference plane bisecting tunnel and bottom-camera lens, parallel to plane of film of side camera when side camera is undeflected (that is, when side camera is aimed at center line of tunnel in plane P_H, see fig. 19)

$s_{H,c}$ horizontal projection of distance from Q to side-camera lens, positive when lens is toward tunnel (fig. 17), ft

$s_{V,c}$ vertical projection of distance between line of sight of side camera to point on model or wall and P_H, positive when lens is deflected above P_H (fig. 17), ft

η deflection from horizontal of line from side-camera lens to a specific point on model, positive when above P_H (figs. 16 and 19), deg

λ deflection from P_V of plane which intersects P_V in a horizontal line passing through center of bottom-camera lens and which contains a specific point on model, positive when deflected toward side camera (figs. 18 and 19), deg

ϵ horizontal projection of angle between a line from Q to a specific point on model and a vertical reference plane perpendicular to P_V (figs. 18 and 19), deg

s_V vertical distance between a specific point on model and P_H, positive when point on model is above P_H (fig. 19), ft

s_H horizontal projection of distance between a specific point on model and Q (fig. 19), ft

s_H' projection of s_H in direction perpendicular to P_V (fig. 19), ft

ρ_H radius vector of polar coordinate system locating center of gravity of model in horizontal plane from center line of tunnel, ft

$\rho_{H,f}$ ρ_H as seen on film-magnifier screen (fig. 18), deg

ζ angle of polar coordinate system locating center of gravity of model in horizontal plane in tunnel (fig. 18), deg

ν acute angle between projection of X body axis in a horizontal plane and ρ_H, positive when measured to right of projection of X body axis as seen from a position directly below nose end of X body axis (figs. 18 and 21), deg

B angle in horizontal plane through center of gravity, between intersection of vertical plane through X body axis with horizontal plane and intersection of plane of symmetry with horizontal plane; also, angle in horizontal plane through center of gravity, between intersection of vertical plane through Y body axis with horizontal plane and intersection of YZ body plane with horizontal plane, positive when ϕ is positive (figs. 21 and 22), deg

A angle in horizontal plane through center of gravity, between intersection of vertical plane through Z body axis with horizontal plane and intersection of plane of symmetry with horizontal plane, positive when ϕ is positive (figs. 21 and 22), deg

Subscripts:

n direction of nose end of X body axis

t direction of tail end of X body axis

wr direction of right-wing end of Y body axis

wl direction of left-wing end of Y body axis

top direction of upper end of Z body axis

H projection in horizontal plane

cg center of gravity

A dot over a symbol represents a derivative with respect to time; for example, $\dot{p} = \frac{dp}{dt}$.

The attitude angles θ_e, ψ_e, and ϕ_e (Eulerean-type space angles) as defined and used herein are intended to provide a means of interpreting any changes from the reference attitudes for either an initially erect or an initially inverted spin. Under this general system, the reference attitude for ϕ_e is arbitrarily taken as zero for either an erect or an inverted spin; the model or airplane would go from an erect to an inverted attitude or vice versa if θ_e becomes greater negatively than -90° or if ϕ_e exceeds $\pm 90^\circ$.

APPARATUS AND METHODS

Model

A $\frac{1}{24}$-scale model which was representative of a contemporary fighter design with a 35° sweptback wing was used in the investigation. A three-view drawing and a photograph of the model are shown in figures 2 and 3. Dimensional characteristics of the airplane represented are listed in table I. The model was made of balsa, spruce, and aluminum. Lead ballast was added in such a manner that the model was considered to represent dynamically a corresponding full-scale airplane at an altitude of 15,000 feet. The mass characteristics of the model as ballasted are presented in table II in terms of full-scale values. A remote-control mechanism was installed in the model to actuate the model controls as desired.

Wind Tunnel and Tests

The model spin and recovery were performed in the Langley 20-foot free-spinning tunnel. This tunnel and its operation are generally similar to that described in reference 1 for the Langley 15-foot free-spinning tunnel, the only difference in operation being that the models are launched by hand with rotation instead of being launched mechanically into the vertically rising airstream. The models are launched with the controls set so as to maintain a spin and the tunnel airspeed is adjusted by an operator so that the weight of the model is supported. The model motion evolves into a fully developed spin or ceases rotating and dives in a "no spin." When a spin is obtained, it is observed for a number of turns, after which an attempt is made to effect a recovery from the spin by moving one or more of the model controls to oppose the spinning motion. Angles of attack for which spins are obtained range from about 70° for flat spins to about 30° for steep spins.

Free-spinning-tunnel investigations have shown that, in general, developed spins may be classified as "steady" or "oscillatory" (ref. 2) depending on whether the model appears to be spinning smoothly or oscillating in roll, yaw, and pitch while spinning. The investigations have also shown that the motion following control movement for recovery may range from one in which the model, immediately after control movement, decreases its rate of rotation and noses down rapidly for a recovery to one in which movement of the controls has little or no effect on the spinning motion. In some instances, after controls are moved for recovery, oscillations may occur in the attitude of the model and in its rate of rotation with an overall trend toward a decrease in both rate of rotation and angle of attack which eventually evolves into a steep low-angle-of-attack pull-out dive without rotation ($\dot{\psi}_e$ becomes zero). Recovery, however, is sometimes considered as having been achieved if the model appears to have entered a glide or a roll at an angle of attack below the stall, even though $\dot{\psi}_e$ has not yet been reduced to zero. In some cases, recovery from the spin may be associated with a quick rolling or pitching motion to an inverted attitude; and recovery is considered to have been achieved from the original erect spin regardless of whether $\dot{\psi}_e$ has changed its direction in space. The motion of a specific airplane during a recovery is apparently dependent on the spin motion before the controls are moved, on the particular control manipulation employed for recovery, and on the effectiveness of these controls (refs. 3 to 5).

For the present investigation, it was decided that a spin and a recovery of a type which has been very common in the past would be studied. This was a spin of medium attitude and moderate oscillations, and the recovery was the type in which the model pitched down to a low angle of attack and ceased rotating within a couple of turns after the control was moved in attempting the recovery. Control settings used on the model for the developed spin were elevator neutral, ailerons neutral, and rudder 30° with the spin (corresponding to right rudder pedal forward in a spin turning toward the right-hand side of the airplane pilot). Control manipulation used for recovery was reversal of the rudder to 15° against the spin.

Camera Setup and Determination of Motion

The technique by which the time histories of the attitudes and velocities of the model during the spin and recovery were determined is explained in detail in the appendix. In brief, the technique is as follows: Motion pictures were made of the model spin and recovery test with two cameras operating simultaneously. One camera was mounted at the bottom of the vertical tunnel and pointed upward along the center line of the tunnel; the other camera was at one side of the tunnel and about on a level with the spinning model. Time histories of the space coordinates of the model in the tunnel were obtained by means of timers mounted in view of each camera, suitable reference lines painted on the tunnel walls, and suitable attitude and position readers devised for and used with a magnifying film viewer. Time histories indicating the attitude of the model in space (angles θ_e, ϕ, and ϕ_e), angular velocities (p, q, r, Ω, and $\dot{\psi}_e$), linear velocities (u, v, w, V_R, V_V, and V), and angles of attack and sideslip were calculated and plotted by using the space coordinates and attitude readings as well as tunnel-velocity readings obtained from an airspeed recorder mounted in view of one camera. Also, by means of several spin-geometry relationships, time histories were calculated and plotted for such factors as the inclinations of the axis of resultant rotation and of the resultant wind from vertical (angles κ_{Ω} and κ_{VR}) and from each other (angle σ), and of the inclinations of the axis of resultant rotation with respect to the airplane XZ and XY body planes (angles δ_{Ω} and τ_{Ω}). A plot indicating the number of turns the model had made in space at any time during the 19 seconds (full-scale time) covered by the spin and recovery was also made. All the time-history plots are presented in terms of full-scale values.

RESULTS AND DISCUSSION

The time-history curves of the attitude and velocity variables during the spin and recovery of the model are presented in figures 4 to 13, and motion-picture strips of the spin and recovery as filmed by the side and bottom cameras are presented in figures 14 and 15, respectively. In general, the spin and recovery motion are discussed separately.

As noted previously, the time histories were obtained for about $3\frac{1}{4}$ turns of a medium-attitude developed spin with moderate oscillations. (See figs. 13 to 15.) The average values of θ_e and ϕ portraying the attitude of the model with respect to horizontal (fig. 4) were about -43° (nose below horizontal) and -3° (left wing below horizontal in spin to pilot's right), respectively. The amplitude of the oscillations in θ_e was about $\pm 7^{\circ}$ and that in ϕ about $\pm 7^{\circ}$. The oscillatory motion of the spin was not completely regular, inasmuch as in any given cycle the period and amplitude were not exactly the same as in the preceding or following cycles. Along with the oscillations in θ_e and ϕ, there occurred corresponding changes in the angles of attack and sideslip (fig. 5). The average angle of attack was about 48°. The sideslip was generally negative (outward sideslip, wind coming from left side of plane of symmetry during spin to pilot's right) and averaged about -7° or -8°. The oscillations in β were in phase with those of angle ϕ and of about the same magnitude.

The angular velocity of the model about a vertical reference axis $\dot{\psi}_e$ during the developed spin was about 90° per second (fig. 7). This value increased slightly a few seconds before rudder reversal. The increase apparently was due to changes in the tunnel airstream associated with the usual practice of lowering the model a few feet just before attempting recovery in order to reduce materially the chances of the model crashing into the tunnel wall above the lower safety net. The oscillations noted earlier in the attitude angles of the spin are reflected in the curves for p, q, and r (fig. 8) and in the remaining time-history plots. For example, as may be seen in figure 9, the angle between the axis of resultant rotation and the relative wind varied from almost zero to about 20°. The angle between the axis of resultant rotation and vertical varied from 0° to 17° (fig. 10). The relative wind direction remained within about 10° of vertical (fig. 10); thus, the model center of gravity moved almost directly toward the ground during the spin. The practically earthward direction of the path of the center of gravity of the model during the spin is also shown by the similarity of the curves for V_V and V_R (fig. 11) up to the time of rudder reversal.

As noted previously, a $1\frac{1}{2}$-turn recovery from the spin was obtained by rudder reversal. (See figs. 13 to 15.) The recovery motion required about 5 seconds (full scale). At the beginning of the recovery motion, soon after rudder reversal, an increase became evident in the oscillations of the attitude variables of the spin (figs. 4 and 5). By the time approximately 2 seconds had elapsed (14.7 seconds on time scale) in the recovery attempt, the left wing had moved downward from horizontal far enough so that the outward sideslip reached 30°; this sideslip is 10° more outward than the sideslip reached during the developed spin. At the same time the angle of attack was about 55°. During the next second or so (see fig. 4, 15.8 seconds on time scale), the left wing rolled upward to about 20° above horizontal and the model reached a high inward sideslip of 16° (fig. 5). At the time this upward movement of the left wing was occurring, the nose was pitching downward in space, and the angle of attack was decreasing to about 38°. The attainment of the 16° sideslip represented the first time during the whole spin and recovery that any appreciable inward sideslip was present. Just before the occurrence of the large inward sideslip, the mean rolling velocity p of the model doubled as the oscillations built up; just after the occurrence of the high inward sideslip, a momentary decrease to almost zero occurred in p. With the momentary decrease in p, the nose of the model began to rotate downward (figs. 4 and 5), and the angular velocities r and $\dot{\psi}_e$ began to decrease consistently. When the model reached the stalling angle ($\alpha = 16°$, based on unpublished results of static-force tests on a model at low Reynolds number) about 2 seconds after the high inward sideslip was obtained, the values of r and $\dot{\psi}_e$ had decreased appreciably and during the next $\frac{1}{2}$ second or so, they reached zero. The recovery from the spin appeared to have been completed at a time of about 5 seconds after rudder reversal when the angle of attack decreased to below the stall. From examination of figure 11, it appears that no appreciable changes occurred in the resultant velocity V_R and rate of descent V_V during most of the recovery beyond those changes which were also present in the developed spin of the model in the tunnel and which represent relatively small changes in tunnel velocity necessary to support the model. Near the end of the recovery V_V decreased somewhat whereas V_R did not; this result would be expected since the model appeared to be pulling out into a glide (figs. 14 and 15) as the recovery was completed.

As an aid in further discussions of the results obtained, it is convenient to consider the spin and recovery in terms of the equations of motion about and along the three body axes. These equations are as follows:

$$I_X\dot{p} = \frac{{V_R}^2\rho Sb}{2} C_l + \left(I_Y - I_Z\right)qr + \dot{r}I_{XZ} + pqI_{XZ} \tag{1}$$

$$I_Y\dot{q} = \frac{{V_R}^2\rho Sb}{2} C_m + \left(I_Z - I_X\right)rp - \left(p^2 - r^2\right)I_{XZ} \tag{2}$$

$$I_Z\dot{r} = \frac{{V_R}^2\rho Sb}{2} C_n + \left(I_X - I_Y\right)pq + \dot{p}I_{XZ} - qrI_{XZ} \tag{3}$$

$$\dot{u} = \frac{{V_R}^2}{2\mu b} C_X - g \sin \theta_e + vr - wq \tag{4}$$

$$\dot{v} = \frac{{V_R}^2}{2\mu b} C_Y + g \cos \theta_e \sin \phi_e + wp - ur \tag{5}$$

$$\dot{w} = \frac{{V_R}^2}{2\mu b} C_Z + g \cos \theta_e \cos \phi_e + uq - vp \tag{6}$$

When p decreased to almost zero just after the large inward sideslip occurred, a corresponding decrease occurred in the gyrodynamic pitching moment (second term on right-hand side of eq. (2)); this decrease apparently had a large effect on the termination of the spinning motion. This effect appears logical because the gyrodynamic pitching moment is the only moment which continuously tends to hold a model or an airplane in a nose-up spinning attitude in balance to the always negative aerodynamic pitching moment. The rolling and yawing gyrodynamic moments are alternately positive and negative during spins and change with q as it oscillates above and below zero (see fig. 8 and eqs. (1) and (3)), and the aerodynamic rolling and yawing moments are likewise alternately positive and negative as they seek to balance the gyrodynamic moments. The products of inertia (eqs. (1) to (3)) are relatively insignificant since body axes and principal axes almost coincide.

The large decrease which occurred in p just after the large inward sideslip was attained could have been due primarily to a relatively large negative aerodynamic rolling moment which was probably present. That such a rolling moment was present has been indicated by an examination of specific numerical values of the various terms in equation (1) at the time the high inward sideslip was present. Making this examination required graphical differentiation of the time-history curve for p to obtain a value for the acceleration term. The value of the acceleration term was of limited accuracy because this differentiation was the second of two graphical differentiations necessary to obtain acceleration data from angular displacement data; however, the results can be taken as a qualitative indication that the magnitude of the negative aerodynamic rolling moment when the high inward sideslip was present was appreciably large. The gyrodynamic rolling moment present at the same time was also negative (q, positive; fig. 9; time, 15.7 sec). This negative gyrodynamic rolling moment was apparently a secondary factor also contributing to the large decrease in p and hence to the large decrease in the gyrodynamic pitching moment.

The probable existence of a large negative aerodynamic rolling moment for the subject model at the time (15.7 seconds on time scale) α was 38°, β was 16°, and p was large is indicated by unpublished results of static rolling-moment measurements and damping-in-roll tests of various sweptback-wing configurations similar to the subject model. The static and damping tests indicated stabilizing dihedral effect and roll damping. For other wing configurations, such as highly sweptback, delta, or unswept wings, the values of dihedral effectiveness and of roll damping may be very different from those for the subject configuration. Therefore, the recovery motion for other configurations may not occur in a manner similar to that of the subject model. It is of interest, however, to note that, for one unswept-wing model with mass loading generally similar to that of the subject model, the apparent importance of a large amount of inward sideslip on a recovery obtained by rudder reversal has been noted in a recent investigation (ref. 6) in which a recovery motion was calculated by using rotary-balance data.

CONCLUDING REMARKS

A technique for determining time histories of the attitudes and velocities of free-spinning-tunnel models during spins and recoveries has been devised and presented. The technique utilizes film taken by two simultaneously operating motion-picture cameras, one mounted at the side and one at the bottom of the vertical tunnel. As an initial application of the technique, time histories have been determined and presented for one medium-attitude, moderately oscillatory developed spin and the recovery therefrom for a model representative of a contemporary fighter airplane.

The results of the investigation indicated that the oscillatory motion of the spin was not completely regular inasmuch as the period and amplitude of any one cycle of the time-history curves were not exactly the same as those for the preceding and following cycles. After rudder reversal, increases occurred in the oscillations, particularly in the angles of wing tilt and sideslip and the recovery was completed about $1\frac{1}{2}$ turns after the rudder was reversed. One factor which apparently had a significant part in the recovery motion obtained in this investigation was a relatively high inward sideslip reached during the oscillations. This sideslip apparently was the primary cause of a sudden large decrease in rolling velocity; this decrease caused a corresponding large decrease in the gyrodynamic pitching moment which had been holding the model in a nose-up spinning attitude.

Langley Aeronautical Laboratory,
National Advisory Committee for Aeronautics,
Langley Field, Va., November 7, 1955.

APPENDIX

TECHNIQUE OF DETERMINING TIME HISTORIES OF ATTITUDES AND VELOCITIES OF MODEL DURING SPIN AND RECOVERY MOTIONS

The motion-picture camera at the bottom of the tunnel was a 35-millimeter camera with a wide-angle lens. This camera was aimed vertically upward along the center line of the tunnel and was not moved from this attitude as it photographed the motion of the model. The camera at the side of the tunnel was a 16-millimeter camera which was yawed and pitched as necessary to follow the motion of the model. The two cameras were not mechanically synchronized but both recorded accurately the passage of time by means of timing devices located in their views.

From film from the side camera, readings of the angle η for four points on the model for numerous times were obtained. These four points are the nose and tail ends of the X body axis and the right and left wing tips. The angle η readings were obtained by making use of lines painted on the tunnel-wall panels behind the model. (See sketch, fig. 16.) In making the trigonometric calculations necessary for laying out points through which these η lines (fig. 16) were painted on the walls, consideration was given to the dimensions of the tunnel (dodecagonal cross section) and to the distances of the side-camera lens from the reference horizontal plane P_H and from a vertical reference line through point Q when the camera was pitched η° and yawed arbitrarily. These latter distances varied with η in accordance with the relationships

$$s_{H,c} = 0.1544 \cos \eta - 0.7500 \sin \eta \tag{7}$$

and

$$s_{V,c} = 0.1544 \sin \eta - 0.7500 (1 - \cos \eta) \tag{8}$$

(See sketch, fig. 17.)

From film from the bottom camera, readings at numerous instants were obtained for the angles λ and ϵ for the same aforementioned four points on the model for which η was read. Readings were also obtained from the film from the bottom camera for the angles ψ_e, ν, and ζ and the distance $\rho_{H,f}$. The sketch in figure 18 illustrates these angles and distances as they appear on the film. Special clear plastic templates were designed and made to enable the reading of these factors on the film with an available magnifying film viewer.

The η readings from the film from the side camera were synchronized with the film readings from the bottom camera timewise by plotting the η readings against time and picking off values for the same instants at which the bottom-camera film readings were made. Then, values of s_V for the four aforementioned points on the model were calculated by use of the equation

$$s_V = \frac{(10.95 - 23.48 \tan \lambda - s_{H,c} \cos \epsilon)\tan \eta + s_{V,c} \cos \epsilon}{\cos \epsilon + \tan \lambda \tan \eta} \tag{9}$$

which is derived as follows: Reference to the sketch in figure 19 indicates that

$$\tan \eta = \frac{s_V - s_{V,c}}{s_H - s_{H,c}} \tag{10}$$

and

$$\tan \lambda = \frac{10.95 - s_H'}{23.48 + s_V} \tag{11}$$

From equation (10),

$$s_H = \frac{s_V - s_{V,c}}{\tan \eta} + s_{H,c}$$

and, as may be seen from figure 19,

$$s_H' = s_H \cos \epsilon = \left(\frac{s_V - s_{V,c}}{\tan \eta} + s_{H,c}\right)\cos \epsilon \tag{12}$$

From equation (11),

$$s_H' = 10.95 - \left(23.48 + s_V\right)\tan \lambda \tag{13}$$

Equating the right-hand sides of equations (12) and (13), expanding, and rearranging gives equation (9).

The attitude angles of the model in space were calculated by the relationships

$$\theta_e = \sin^{-1} \frac{s_{V,t} - s_{V,n}}{l} \tag{14}$$

$$\phi = \sin^{-1} \frac{s_{V,wl} - s_{V,wr}}{b} \tag{15}$$

and

$$\phi_e = \sin^{-1} \frac{\sin \phi}{\cos \theta_e} \tag{16}$$

(See fig. 20.) (It is of interest to note here that, if a model were to be in an inverted attitude rather than in an erect attitude, equation (15) would take the form $\phi = \sin^{-1} \frac{s_{V,wr} - s_{V,wl}}{b}$.) The angular velocities p, q, and r were calculated from

$$p = \dot{\phi}_e - \dot{\psi}_e \sin \theta_e \tag{17}$$

$$q = \dot{\theta}_e \cos \phi_e + \dot{\psi}_e \cos \theta_e \sin \phi_e \tag{18}$$

and

$$r = -\dot{\theta}_e \sin \phi_e + \dot{\psi}_e \cos \theta_e \cos \phi_e \tag{19}$$

(angular velocities about body axes in terms of Eulerean-type space angles similar to those of ref. 7). Values of $\dot{\phi}_e$, $\dot{\theta}_e$, and $\dot{\psi}_e$ were obtained graphically from ϕ_e, θ_e, and ψ_e. Values of the resultant angular velocity Ω were obtained by vectorial addition of the mutually perpendicular angular velocities p, q, and r.

The linear velocities u, v, and w were calculated by the following equations:

$$u = \pm \frac{d\rho_H}{dt} \cos \nu \cos \theta_e + \frac{d\zeta}{dt}\rho_H \sin \nu \cos \theta_e - V_V \sin \theta_e \tag{20}$$

$$v = -\frac{d\rho_H}{dt}\sin(\nu \pm B)\cos\phi \pm \frac{d\zeta}{dt}\rho_H\cos(\nu \pm B)\cos\phi + V_V\sin\phi \tag{21}$$

$$w = \mp\frac{d\rho_H}{dt}\cos(\nu \pm A \pm B)\cos\alpha_3 - \frac{d\zeta}{dt}\rho_H\sin(\nu \pm A \pm B)\cos\alpha_3 + V_V\cos\theta_e\cos\phi_e \tag{22}$$

When a choice of signs is indicated in equations (20), (21), and (22), the upper sign applies if $\nu = \nu_t$ and the lower sign applies if $\nu = \nu_n$. As an aid in visualizing the angles used in equations (20), (21), and (22) and the significance of the relationships, refer to the sketches in figure 21. The instructions regarding signs would be different from those used if θ_e were to become positive or if the model were to be in an inverted attitude.

Values of ρ_H for use in equations (20), (21), and (22) were obtained by multiplying the tangent of the angle represented through distance $\rho_{H,f}$ on film-magnifier glass (fig. 18) times the factor $\left(23.48 - s_{V,cg}\right)$. The latter factor represents the vertical distance of the center of gravity of the model above the lens of the bottom camera. Values of $s_{V,cg}$ were determined simply from knowing $s_{V,n}$, $s_{V,t}$, the fuselage length, and the location of the model center of gravity along the fuselage length. Values of $\frac{d\rho_H}{dt}$ and $\frac{d\zeta}{dt}$ were obtained graphically from ρ_H and from ζ. Values of α_3, A, and B were calculated from the relationships (see figs. 20 and 22)

$$\sin\alpha_3 = \cos\theta_e\cos\phi_e \tag{23}$$

$$\sin A = \tan\phi\tan\alpha_3 \tag{24}$$

$$\cos B = \frac{\cos\phi_e}{\cos\phi} \tag{25}$$

Values of V_V were obtained from

$$V_V = V_{tunnel} + \frac{ds_{V,cg}}{dt} \tag{26}$$

where the latter term was determined graphically.

Values of the resultant linear velocity V_R were obtained by vectorial addition of the mutually perpendicular linear velocities u, v, and w. Angles of attack and sideslip were calculated from

$$\alpha = \tan^{-1} \frac{w}{u} \tag{27}$$

and

$$\beta = \sin^{-1} \frac{v}{V_R} \tag{28}$$

The angles between the axis of resultant rotation and the XZ and XY body planes were calculated by

$$\delta_\Omega = \sin^{-1} \frac{q}{\sqrt{p^2 + q^2}} \tag{29}$$

and

$$\tau_\Omega = \sin^{-1} \frac{r}{\Omega} \tag{30}$$

The angle between the axis of resultant rotation and the direction of the resultant wind was calculated by

$$\cos \sigma = \cos \tau_\Omega \cos \tau_{VR} \cos\left(\delta_\Omega - \delta_{VR}\right) + \sin \tau_\Omega \sin \tau_{VR} \tag{31}$$

(See fig. 23.) The velocity along the axis of resultant rotation was calculated by

$$V = V_R \cos \sigma \tag{32}$$

The inclination of the axis of resultant rotation from the vertical was calculated by

$$\cos \kappa_\Omega = \cos \alpha_1' \cos \alpha_1 + \sin \alpha_1' \sin \alpha_1 \cos\left(\cos^{-1} \frac{r}{\sqrt{r^2 + q^2}} \pm \cos^{-1} \frac{\sin \alpha_3}{\sin \alpha_1}\right) \tag{33}$$

which is derived fully in reference 6. Equation (33) represents a spherical trigonometric method for determining κ_Ω and makes use of known values for the attitude of the airplane with respect to the vertical and the inclination of the axis of resultant rotation with respect to the airplane. In the present computation, the negative sign in the last term of equation (33) was used when δ_{Ω} and ϕ were of like sign, and the positive sign was used when δ_{Ω} and ϕ were of opposite sign. The inclination of the resultant linear velocity vector from vertical was calculated from

$$\cos \kappa_{VR} = \frac{V_V}{V_R} \tag{34}$$

The number of turns the model had made in space at any time during the spin and recovery was determined directly from the values of ψ_e read from the film.

It should be noted that extreme care was used in establishing the accuracy with which the film could be read and with which slopes of curves could be taken by graphical procedures. These accuracies were used judiciously in fairing the measured data and the subsequent calculated results.

REFERENCES

1. Zimmerman, C. H.: Preliminary Tests in the N.A.C.A. Free-Spinning Wind Tunnel. NACA Rep. 557, 1936.

2. Stone, Ralph W., Jr., and Klinar, Walter J.: The Influence of Very Heavy Fuselage Mass Loadings and Long Nose Lengths Upon Oscillations in the Spin. NACA TN 1510, 1948.

3. Neihouse, Anshal I., Lichtenstein, Jacob H., and Pepoon, Philip W.: Tail-Design Requirements for Satisfactory Spin Recovery. NACA TN 1045, 1946.

4. Neihouse, A. I.: Tail-Design Requirements for Satisfactory Spin Recovery for Personal-Owner-Type Light Airplanes. NACA TN 1329, 1947.

5. Neihouse, A. I.: A Mass-Distribution Criterion for Predicting the Effect of Control Manipulation on the Recovery From a Spin. NACA WR L-168, 1942. (Formerly NACA ARR, Aug. 1942.)

6. Scher, Stanley H.: An Analytical Investigation of Airplane Spin-Recovery Motion by Use of Rotary-Balance Aerodynamic Data. NACA TN 3188, 1954.

7. MacMillan, William Duncan: Theoretical Mechanics. Dynamics of Rigid Bodies. McGraw-Hill Book Co., Inc., 1936, pp. 184-185.

TABLE I

DIMENSIONAL CHARACTERISTICS OF AIRPLANE REPRESENTED BY MODEL

Overall length, ft	37.5
Wing:	
Span, ft	37.1
Area, sq ft	287.9
Sweepback at quarter chord, deg	35
Dihedral, deg	3
Incidence at root, deg	1
Incidence at tip, deg	-1
Section at root	NACA 0012-64 modified
Section at tip	NACA 0011-64 modified
Aspect ratio	4.8
Mean aerodynamic chord, in.	97.0
Leading edge of $\bar{c}$ rearward of leading edge of root chord, in.	46.0
Ailerons:	
Area, sq ft	39.2
Span, percent semispan	50.1
Hinge-line location, percent chord	70
Horizontal tail:	
Total area, sq ft	35.0
Span, ft	12.8
Sweepback at quarter chord, deg	35
Elevator area rearward of hinge line, sq ft	10.1
Distance from center of gravity to elevator hinge line at root, ft	18.0
Dihedral, deg	10
Incidence, deg	0
Vertical tail:	
Total area, sq ft	33.7
Sweepback at quarter chord, deg	35
Rudder area rearward of hinge line, sq ft	8.7
Distance from center of gravity to rudder hinge line at root, ft	17.3
Unshielded rudder volume coefficient	0.0143
Tail-damping ratio	0.0204
Tail-damping power factor	0.000290

TABLE II.- MASS CHARACTERISTICS FOR MODEL

[Values are given in terms of full-scale airplane; moments of inertia are about center of gravity]

Weight, lb	13,103
μ at an altitude of 15,000 ft	25.45
$\frac{x}{\bar{c}}$	0.221
$\frac{z}{\bar{c}}$	0.133
I_X, slug-ft^2	9,255
I_Y, slug-ft^2	25,859
I_Z, slug-ft^2	33,205
$\frac{I_X - I_Y}{mb^2}$	-296×10^{-4}
$\frac{I_Y - I_Z}{mb^2}$	-131×10^{-4}
$\frac{I_Z - I_X}{mb^2}$	427×10^{-4}

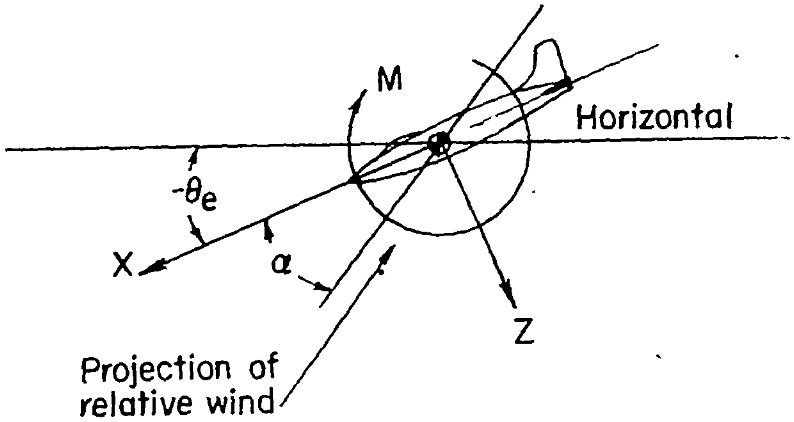

(a) ϕ_e and $\psi_e = 0$.

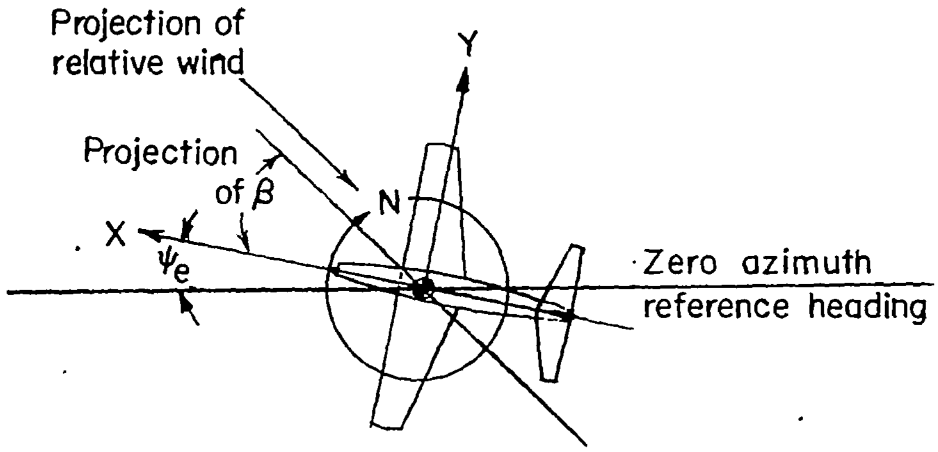

(b) θ_e and $\phi_e = 0$.

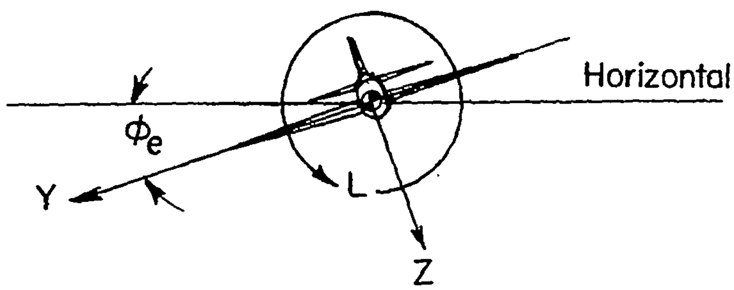

(c) θ_e and $\psi_e = 0$, and in this case $\phi = \phi_e$.

Figure 1.- Body system of axes and related angles.

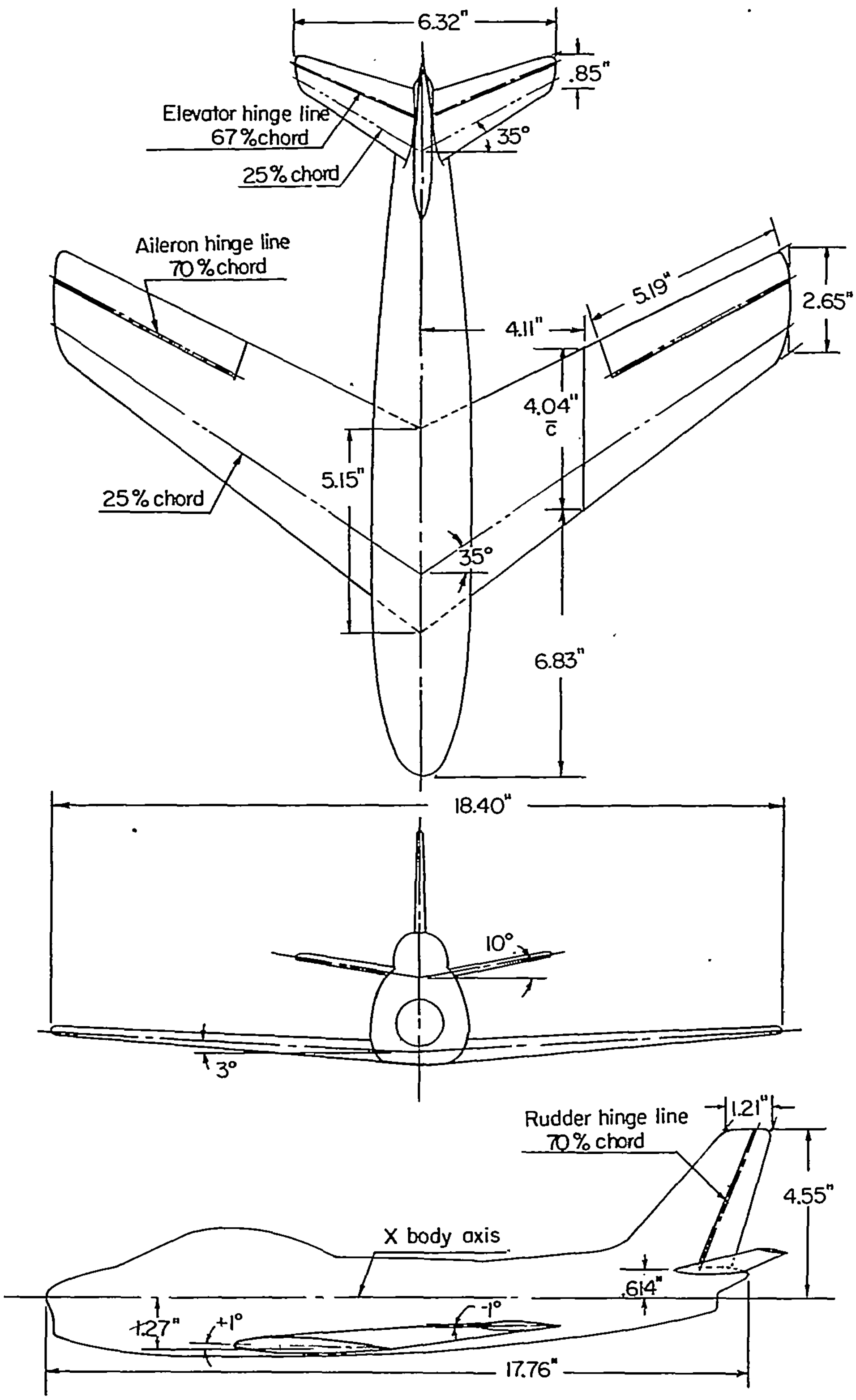

Figure 2.- Three-view drawing of the model.

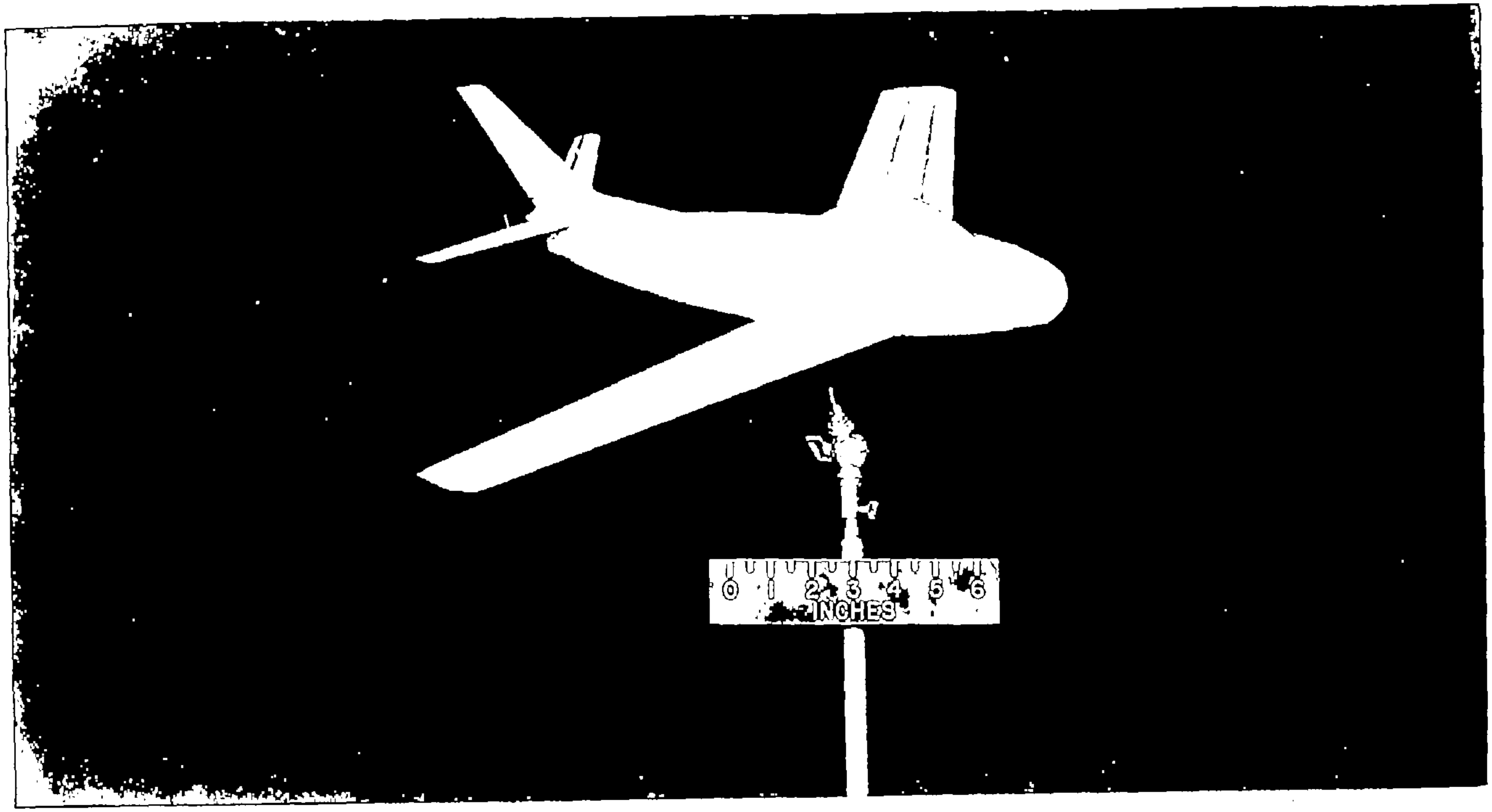

L-79975

Figure 3.- Photograph of the model.

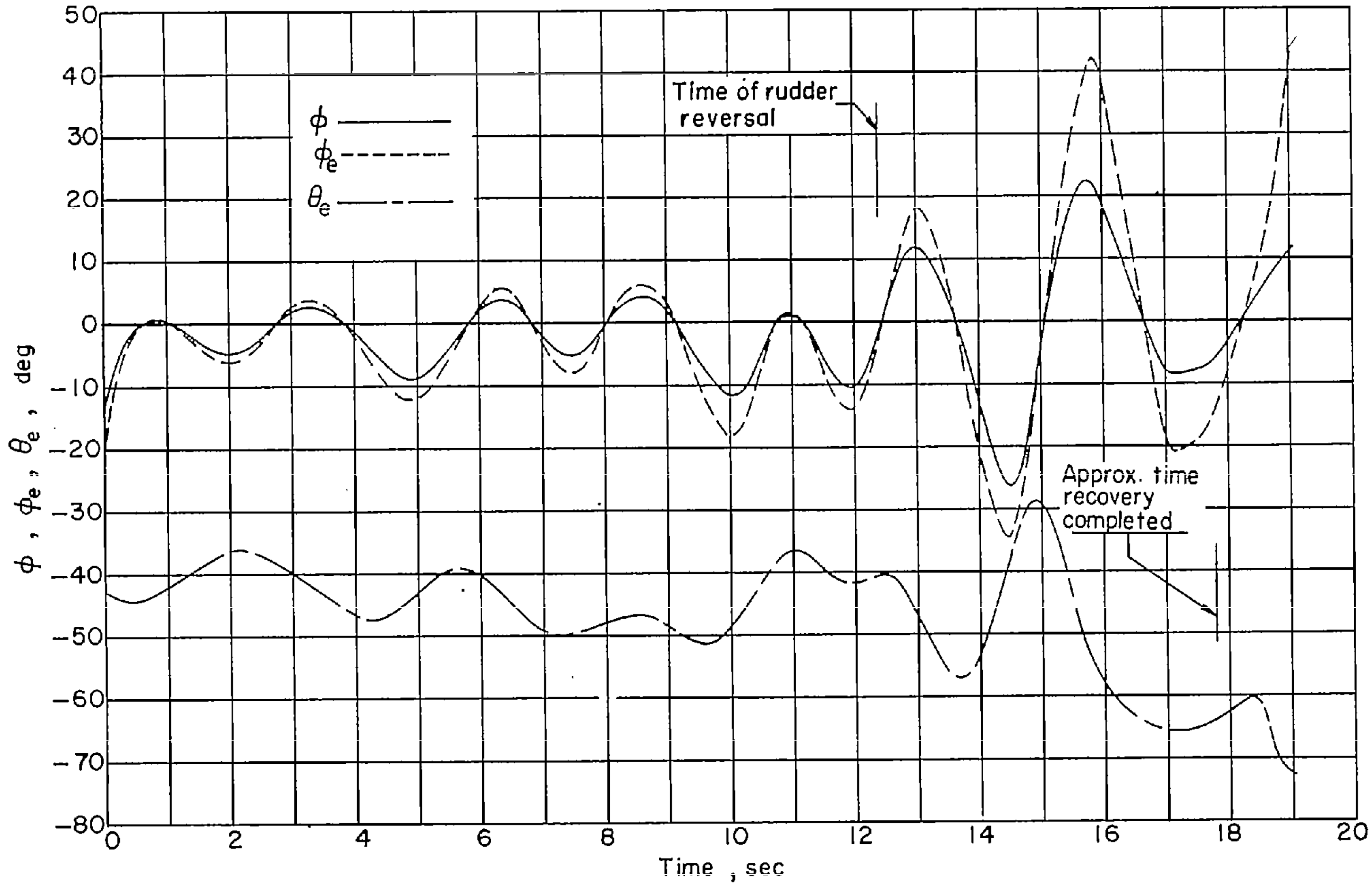

Figure 4.- Variation of attitude angles ϕ, ϕ_e, and θ_e with time during spin and recovery of model.

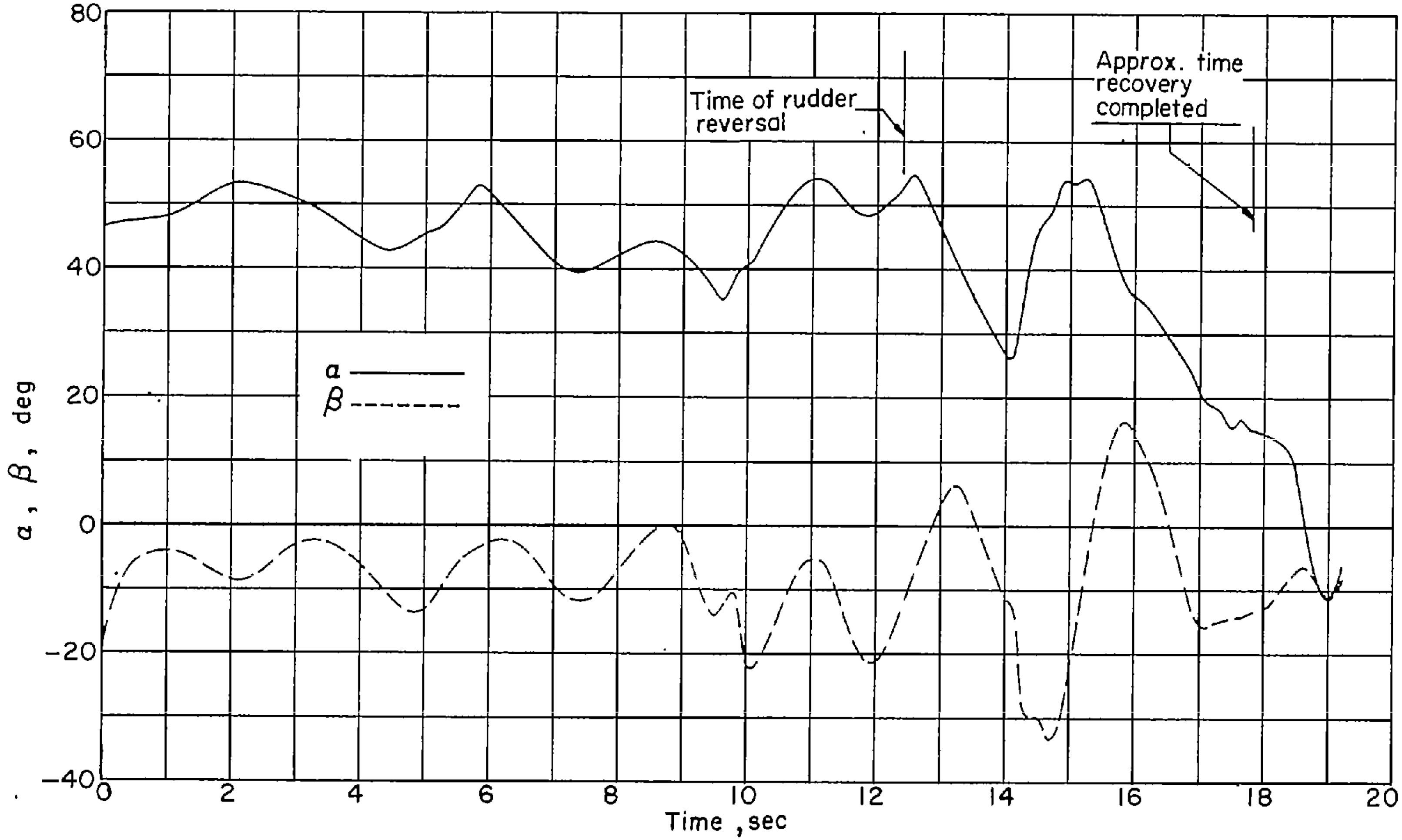

Figure 5.- Variation of angles of attack and sideslip with time during spin and recovery of model.

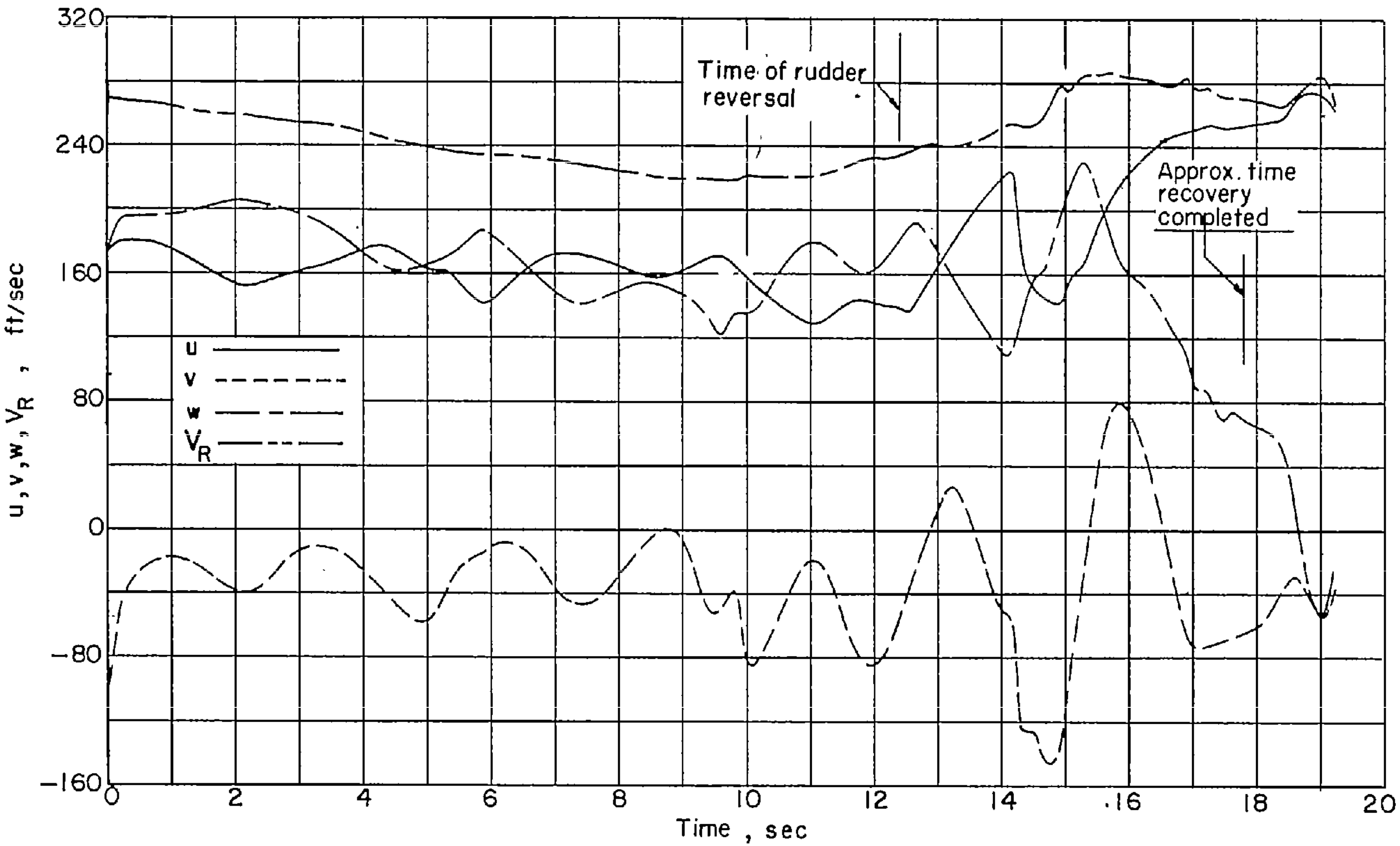

Figure 6.- Variation of linear velocities u, v, w, and V_R with time during spin and recovery of model.

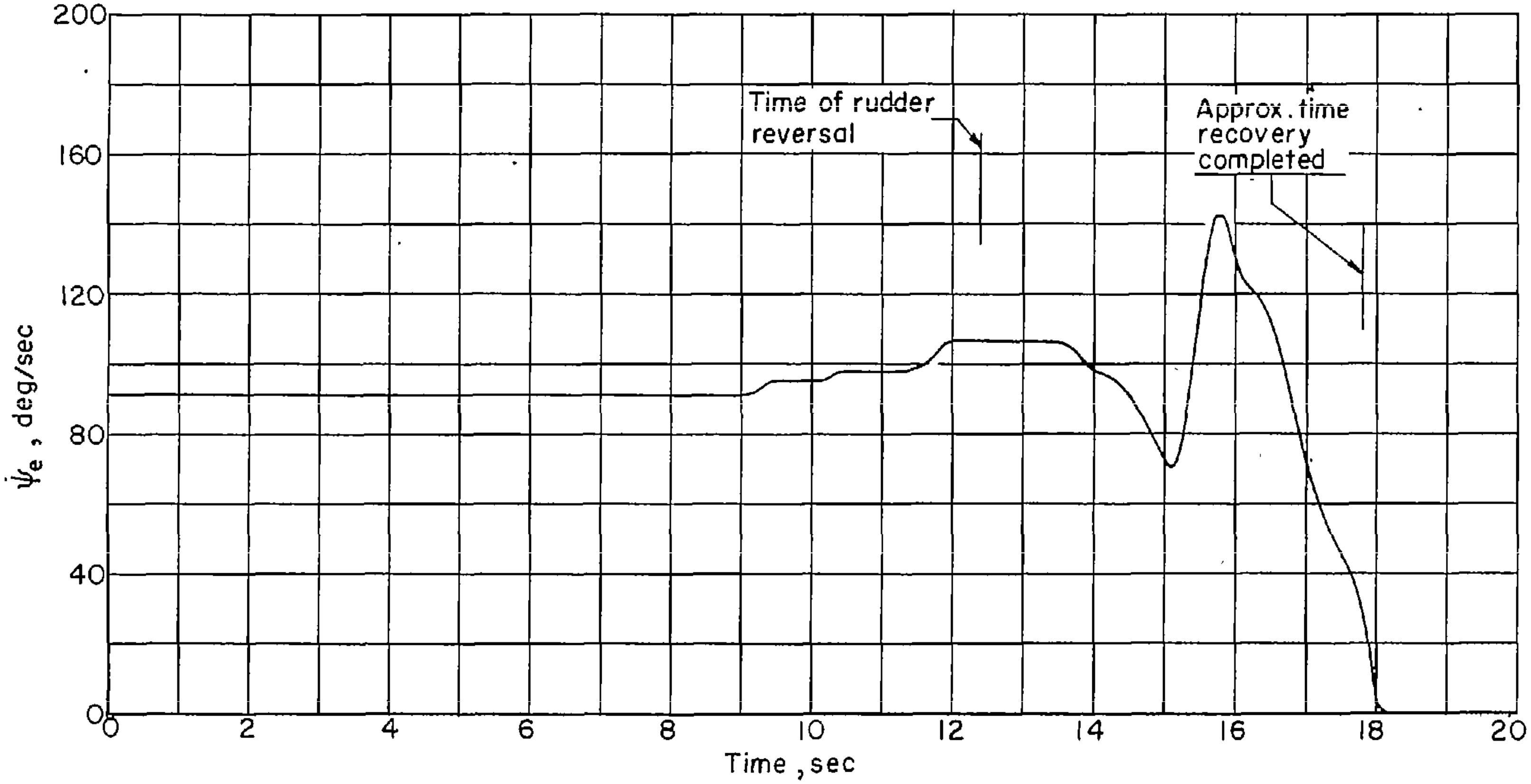

Figure 7.- Variation of rate of rotation about vertical axis with time during spin and recovery of model.

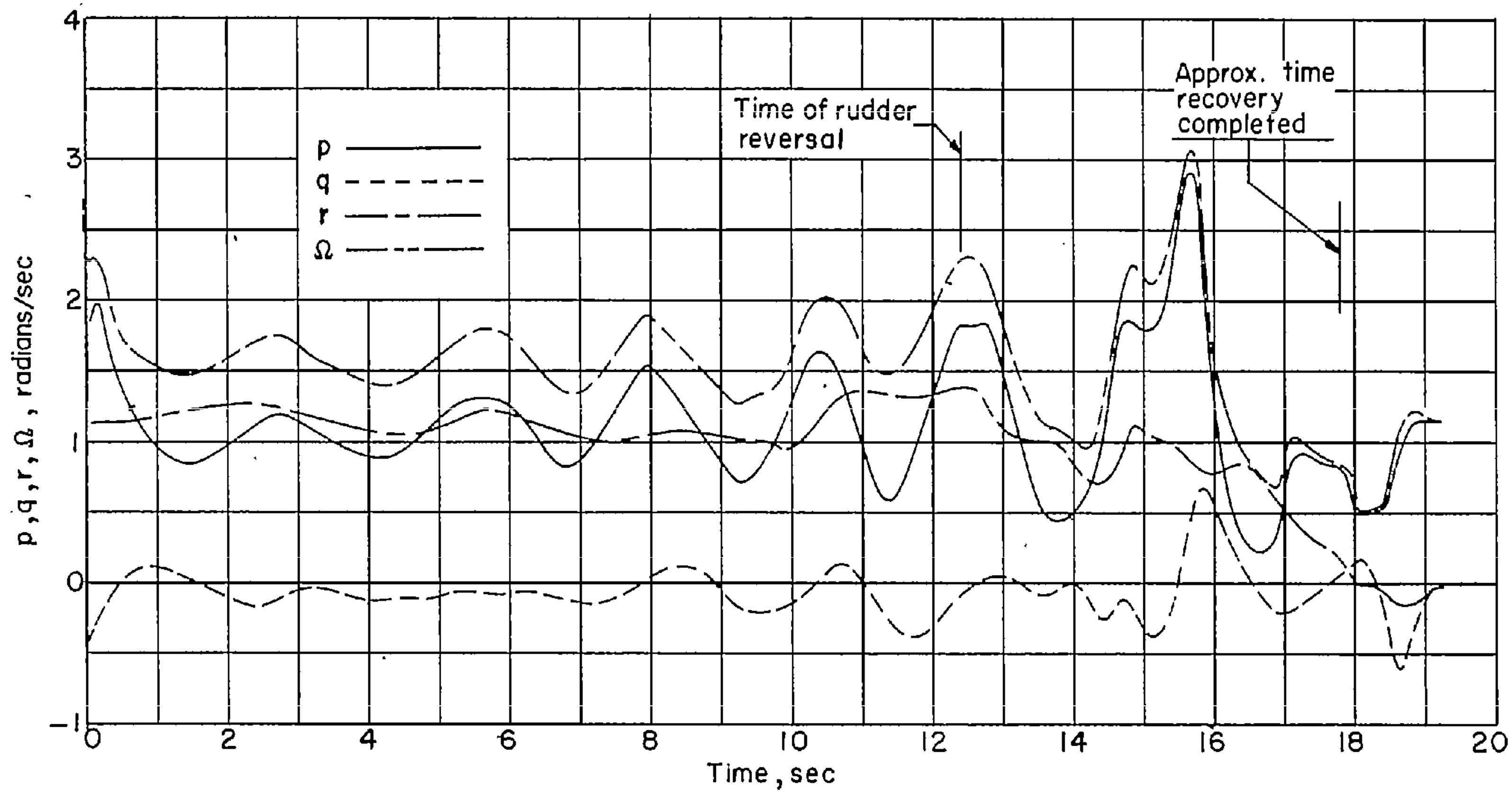

Figure 8.- Variation of angular velocities p, q, r, and Ω with time during spin and recovery of model.

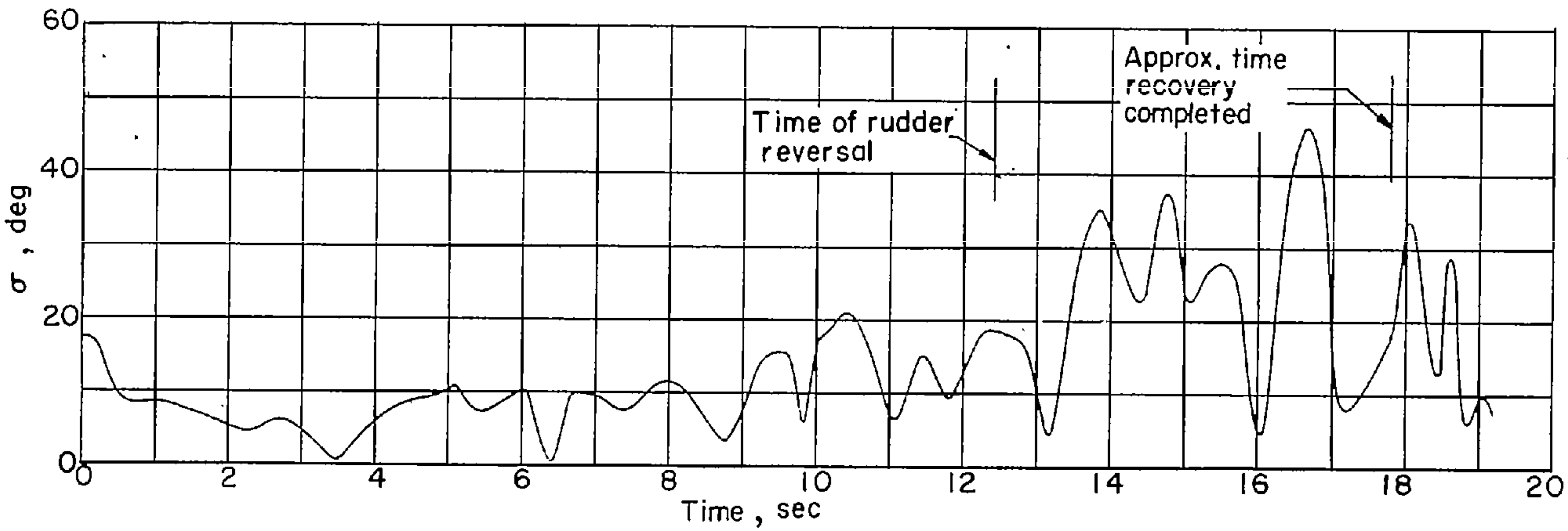

Figure 9.- Variation of angle between relative wind and axis of resultant rotation with time during spin and recovery of model.

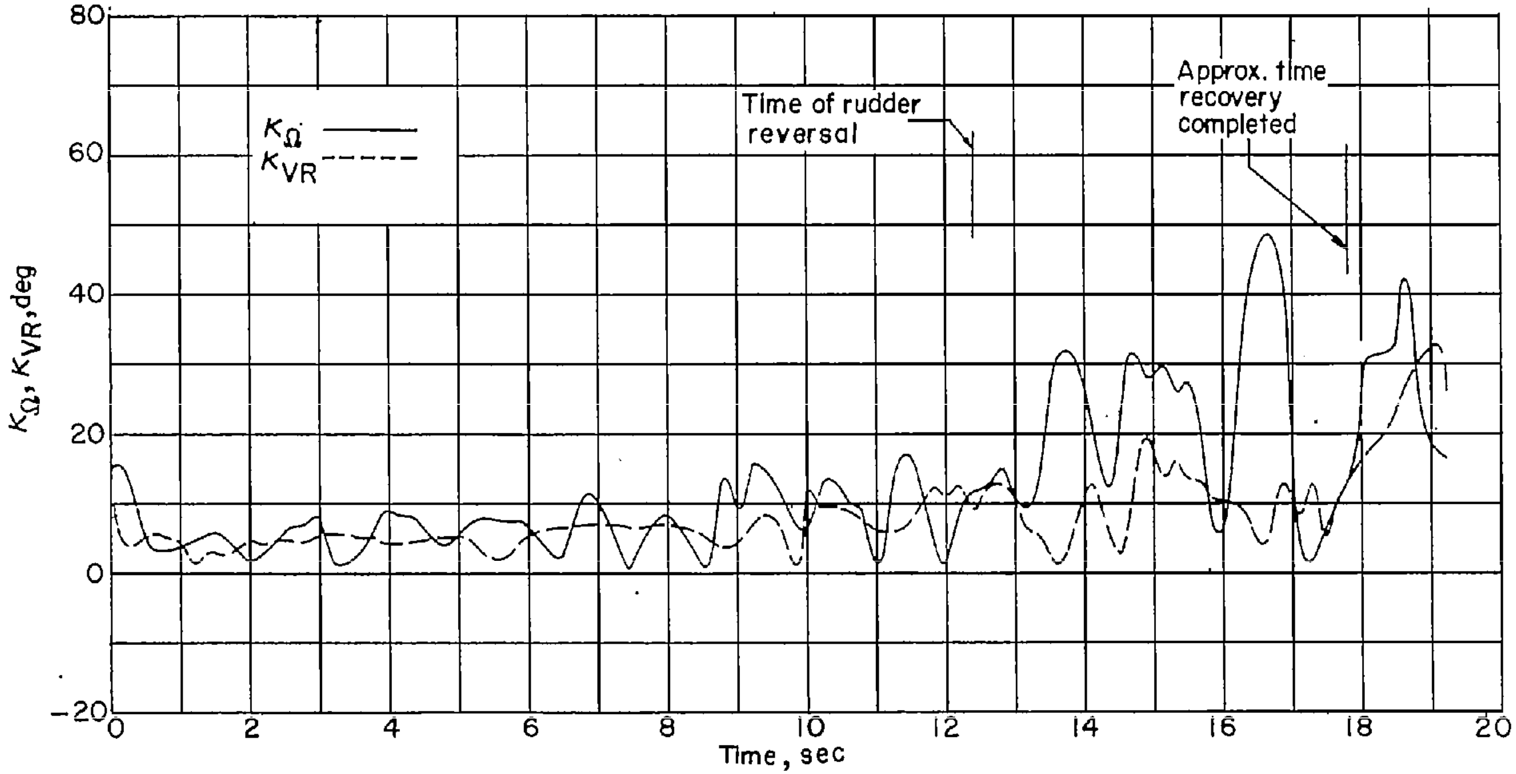

Figure 10.- Variation of angles between axis of resultant rotation and vertical and between relative wind and vertical with time during spin and recovery of model.

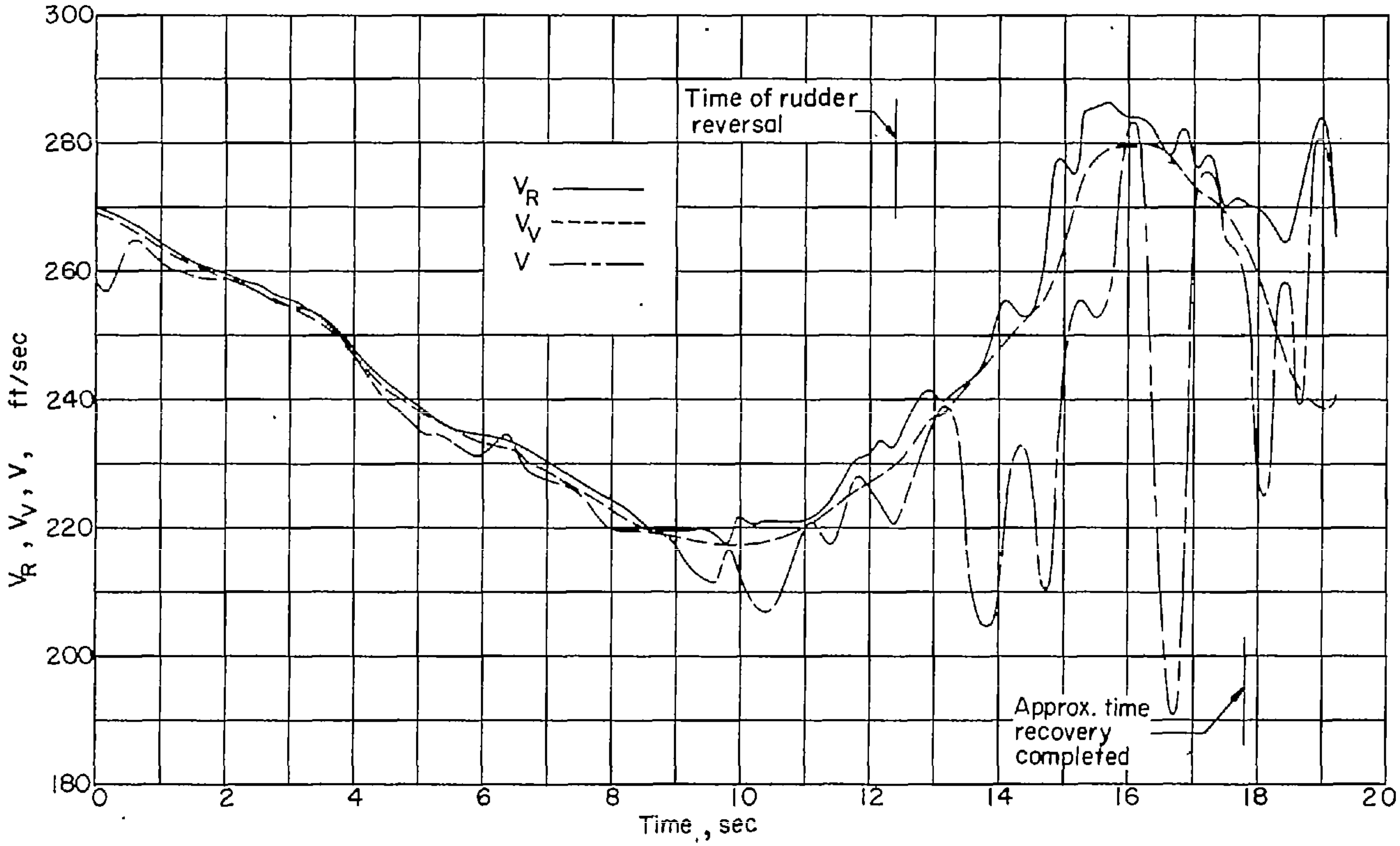

Figure 11.- Variation of linear velocities V, V_V, and V_R with time during spin and recovery of model.

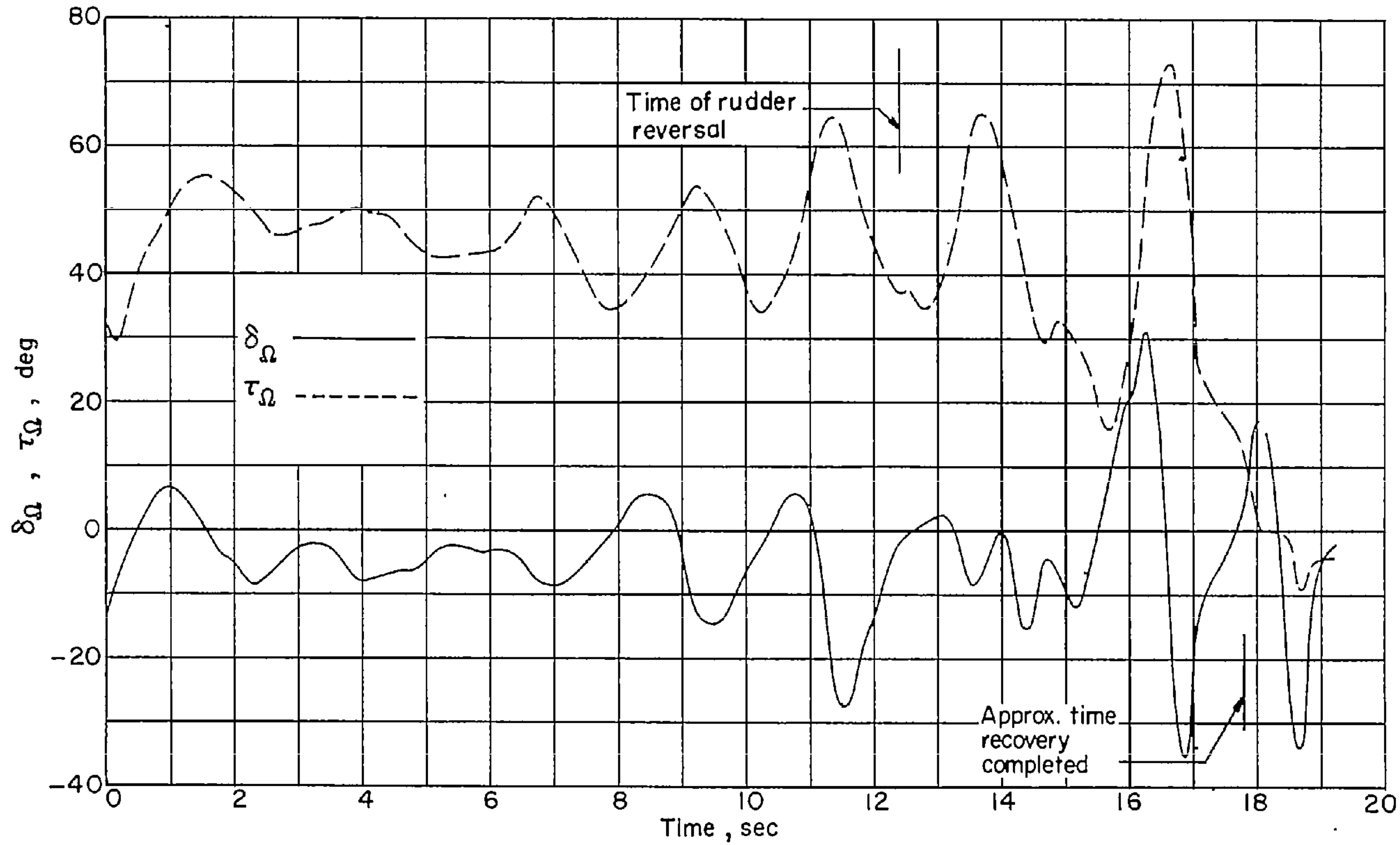

Figure 12.- Variation of angles δ_Ω and τ_Ω (locating axis of resultant rotation with respect to XZ and XY body planes, respectively) with time during spin and recovery of model.

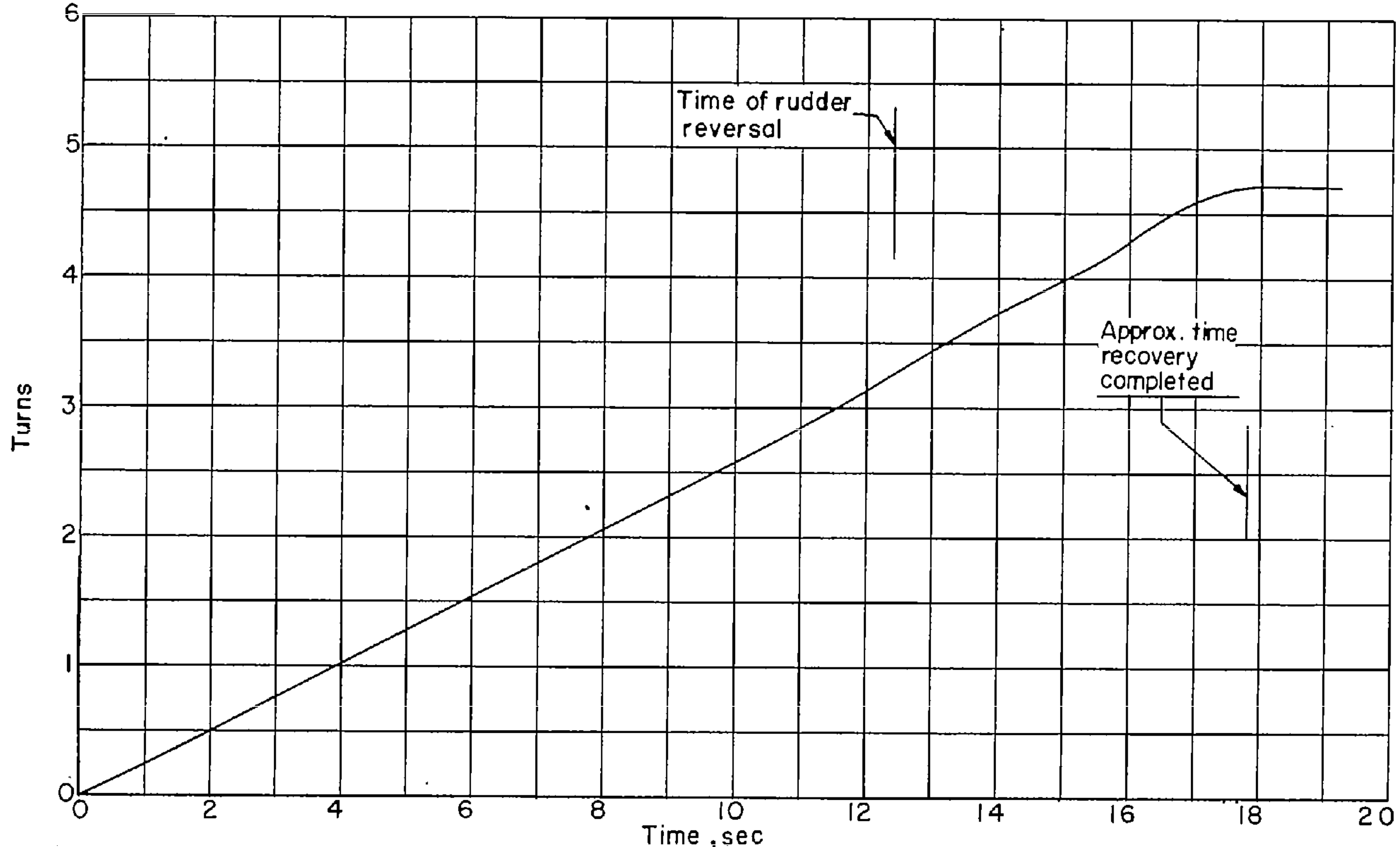

Figure 13.- Variation of turns completed about vertical axis with time during spin and recovery of model.

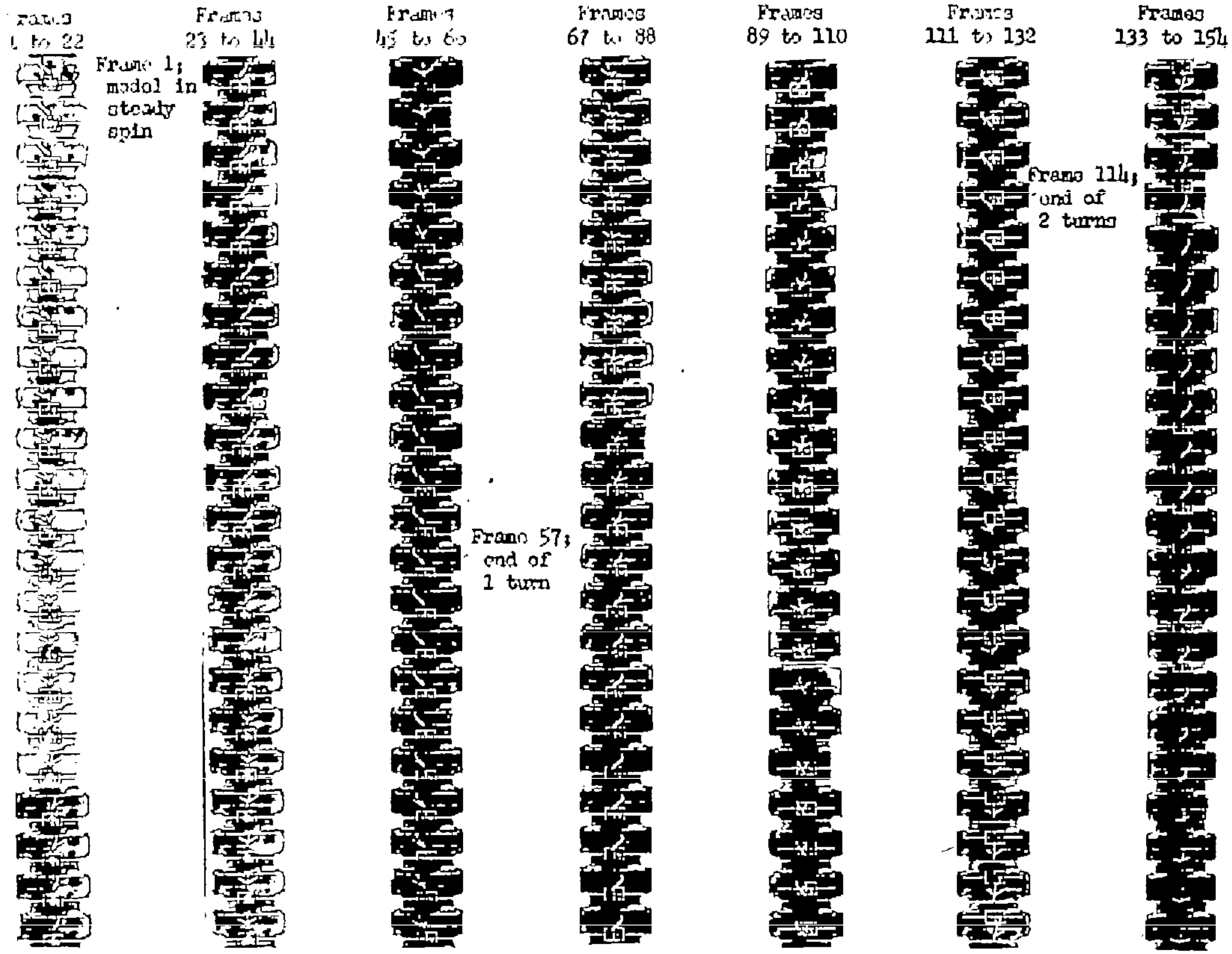

L-90537

Figure 14.- Motion-picture strip of model spin and recovery as filmed from side camera.

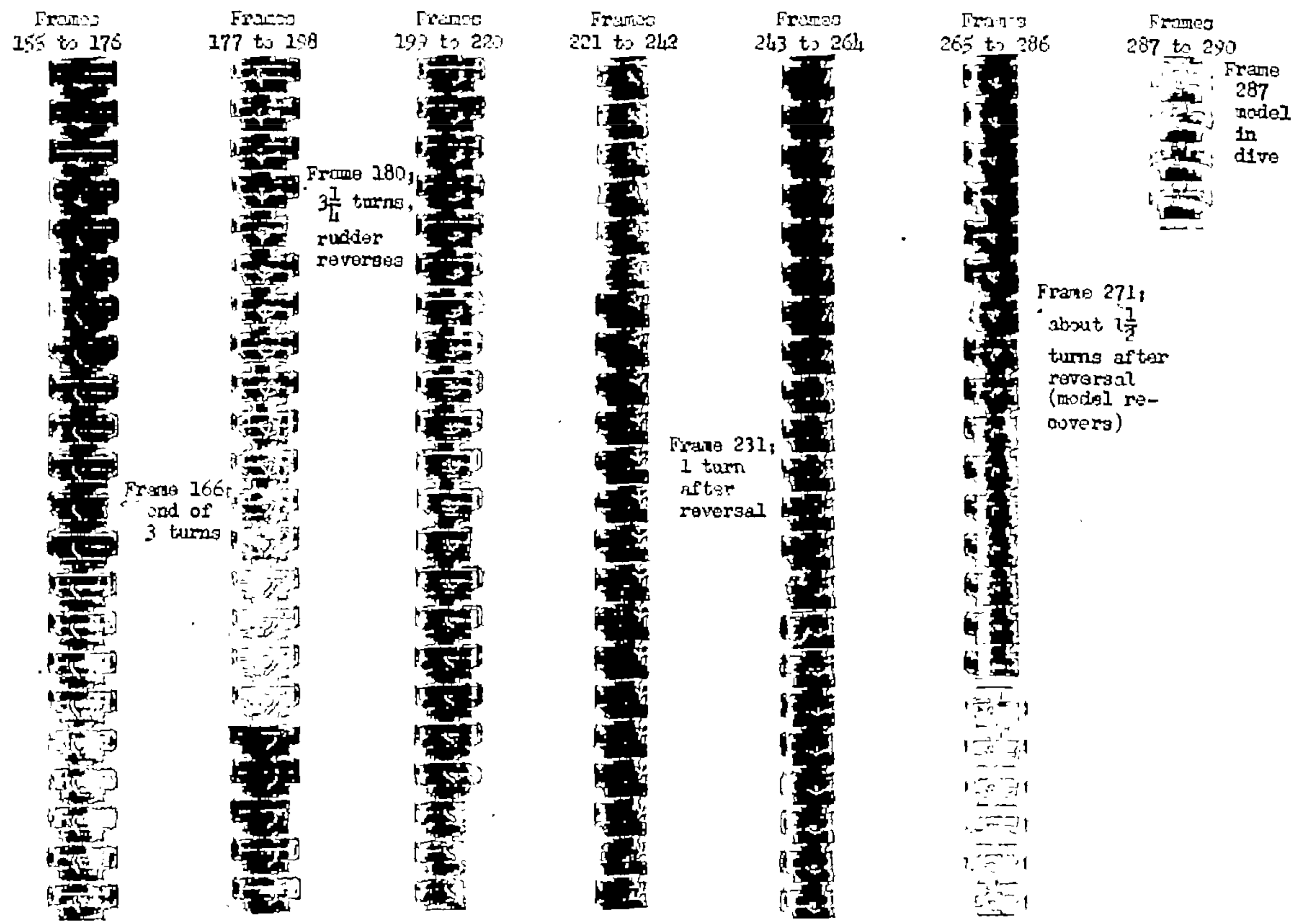

Figure 14.- Concluded.

L-90538

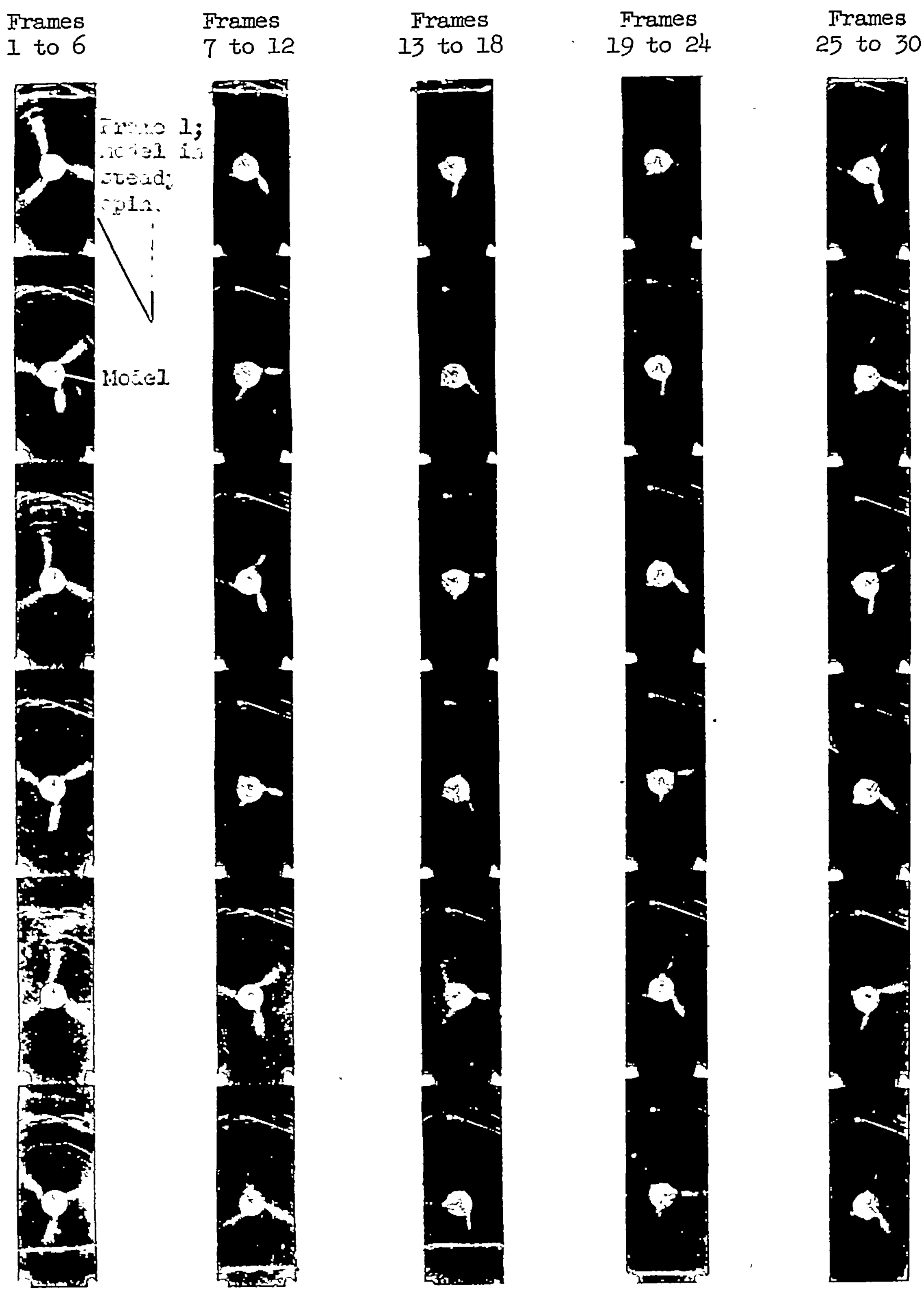

L-90533

Figure 15.- Motion-picture strip of model spin and recovery as filmed from bottom camera.

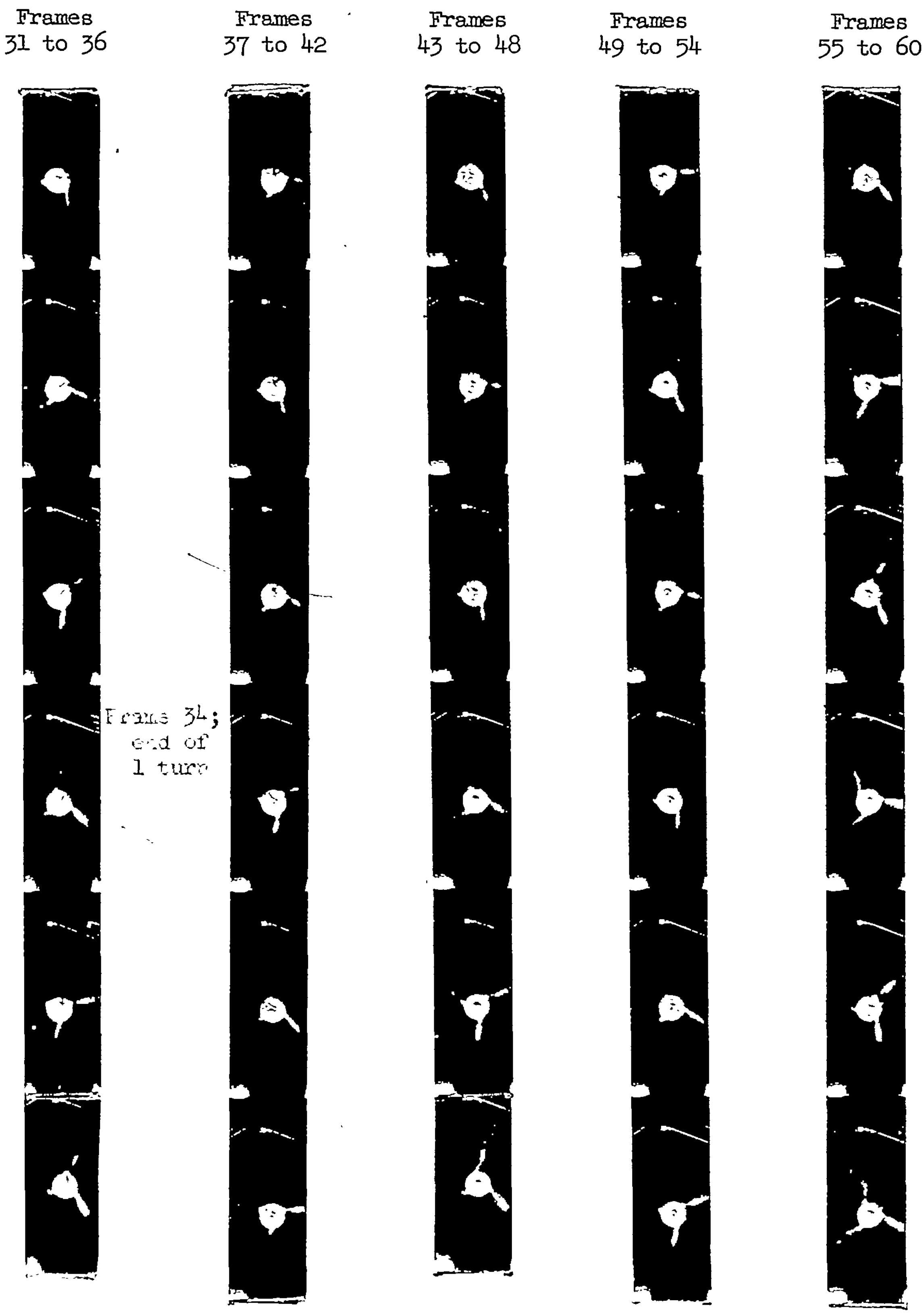

Figure 15.- Continued.

L-90534

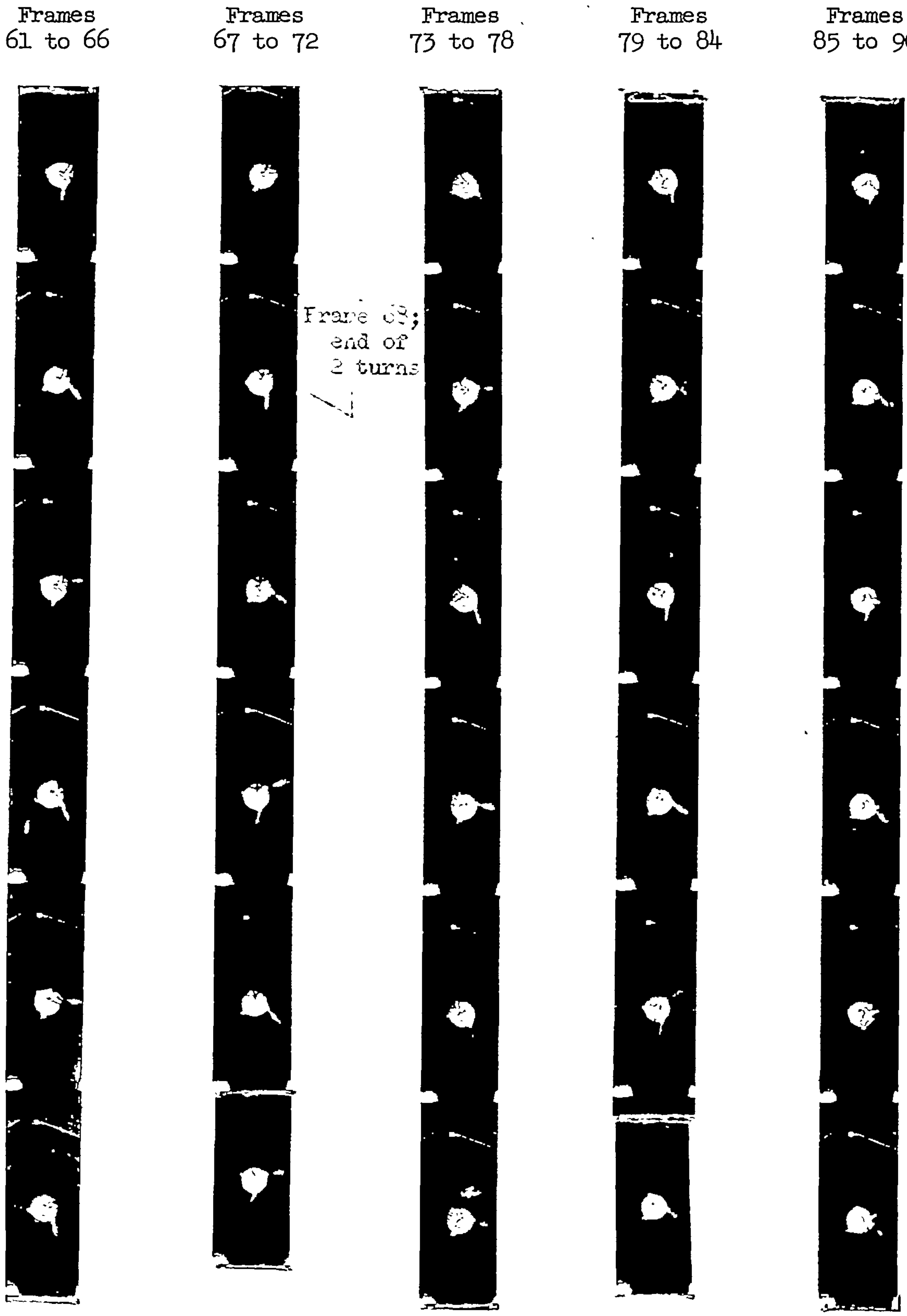

Figure 15.- Continued.

L-90535

Frames 91 to 96	Frames 97 to 102	Frames 103 to 108	Frames 109 to 114	Frames 115 to 120

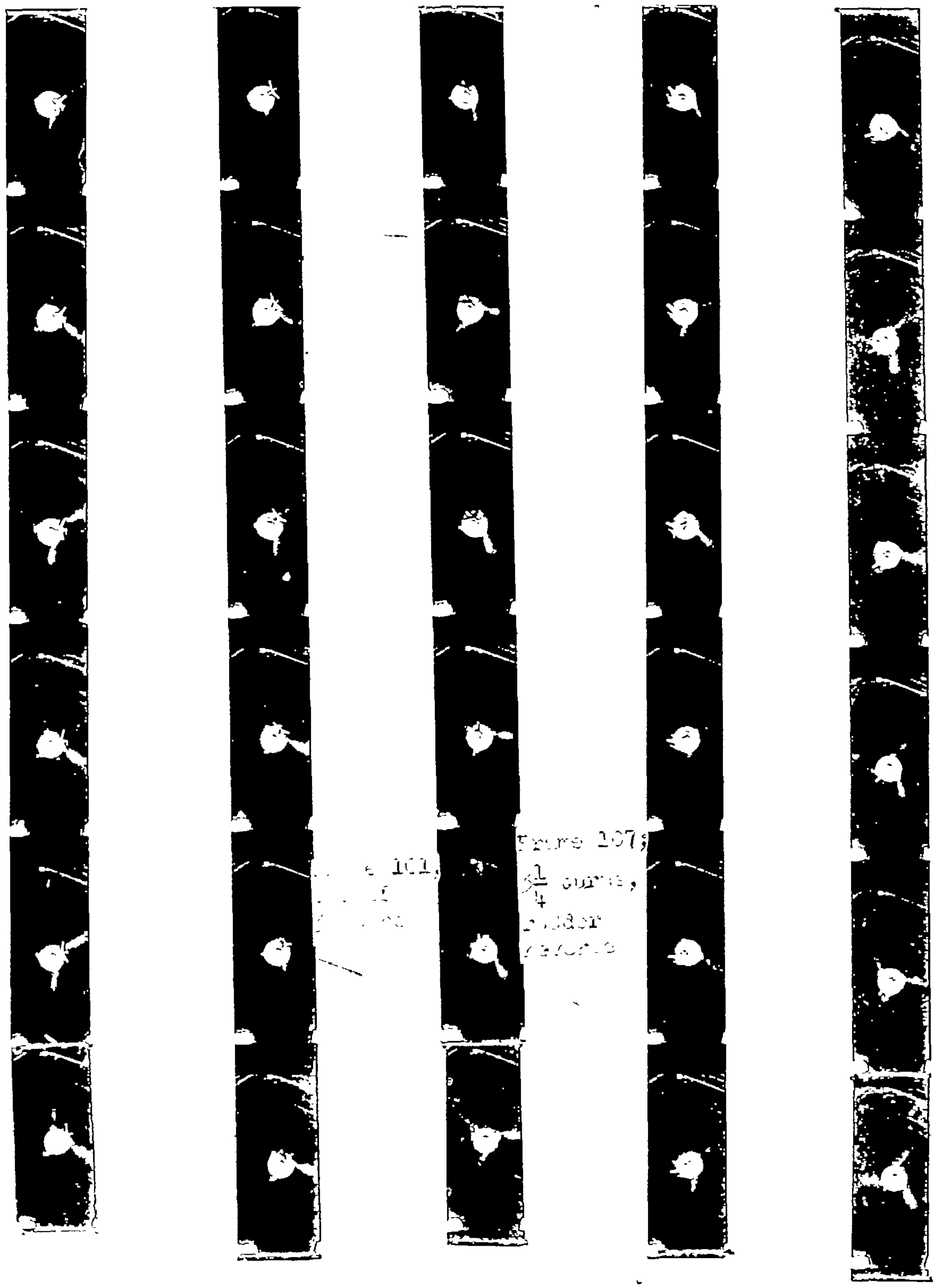

Figure 15.- Continued.

L-90536

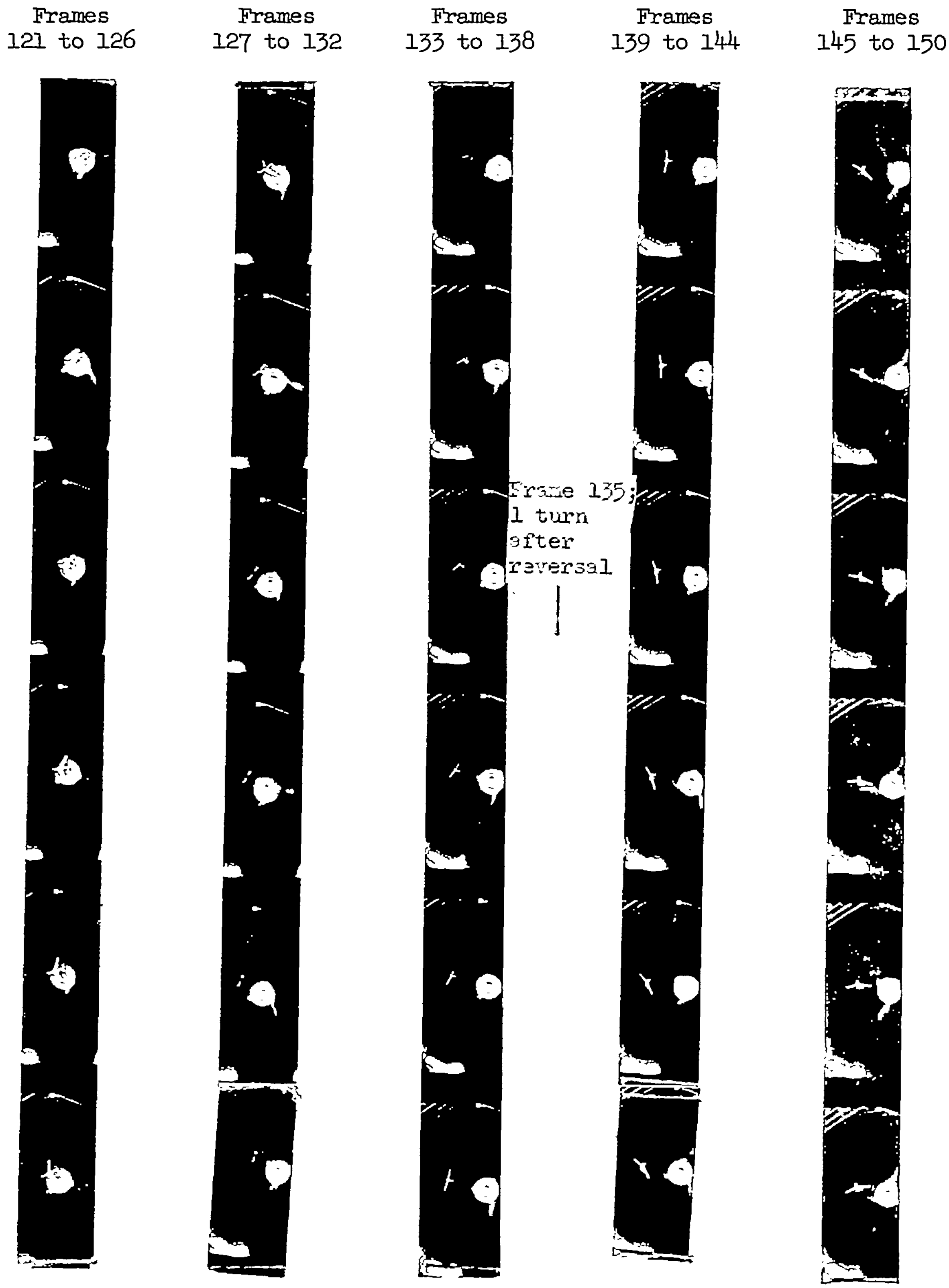

Figure 15.- Continued.

L-91697

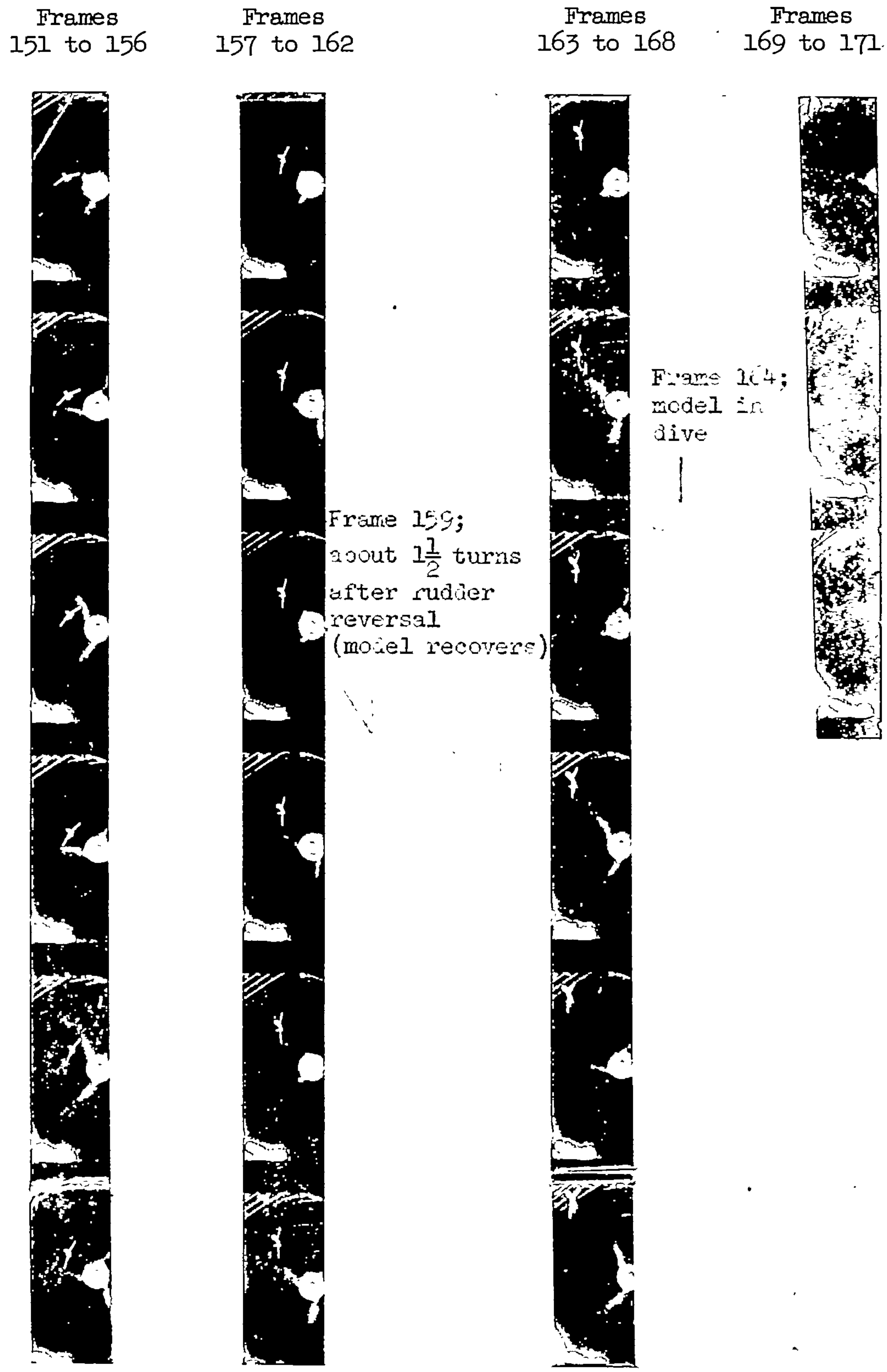

Figure 15.- Concluded.

L-91698

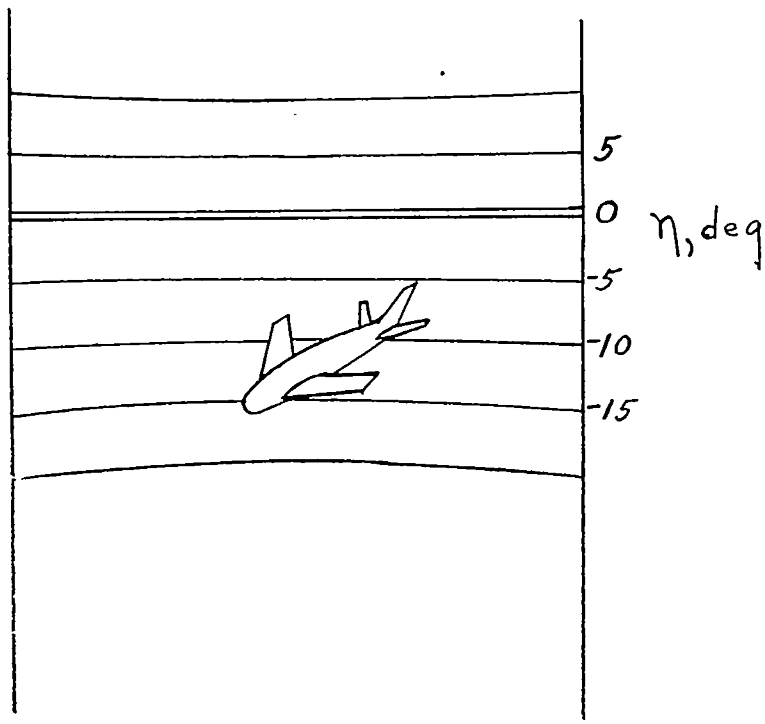

Figure 16.- Sketch indicating model and lines on tunnel walls as seen from film taken by side camera.

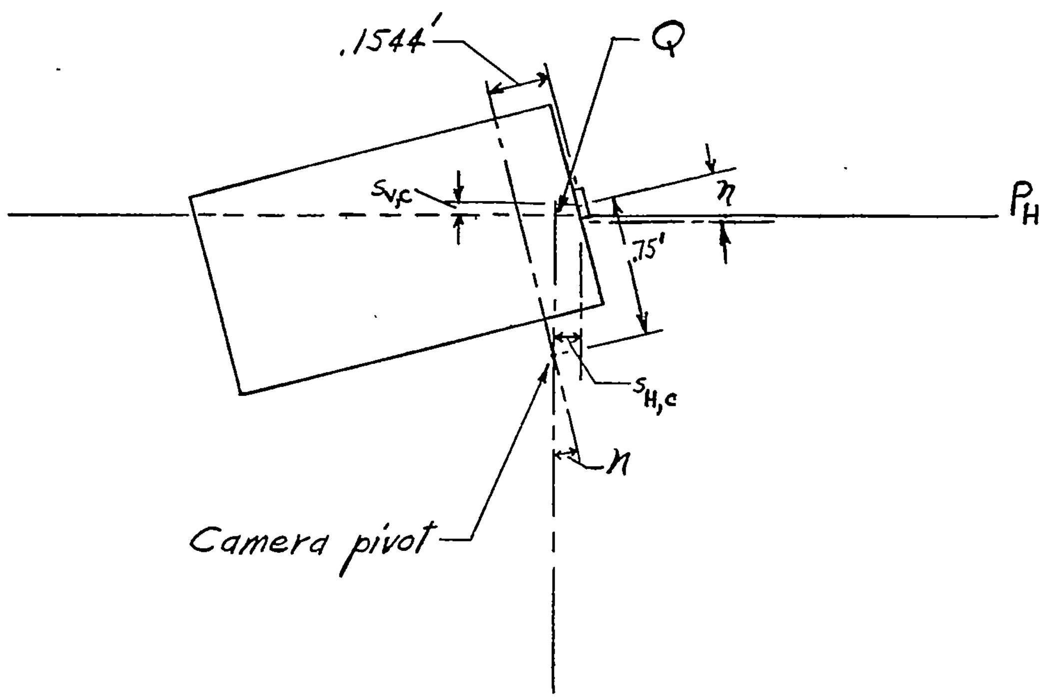

Figure 17.- Sketch indicating pertinent camera dimensions.

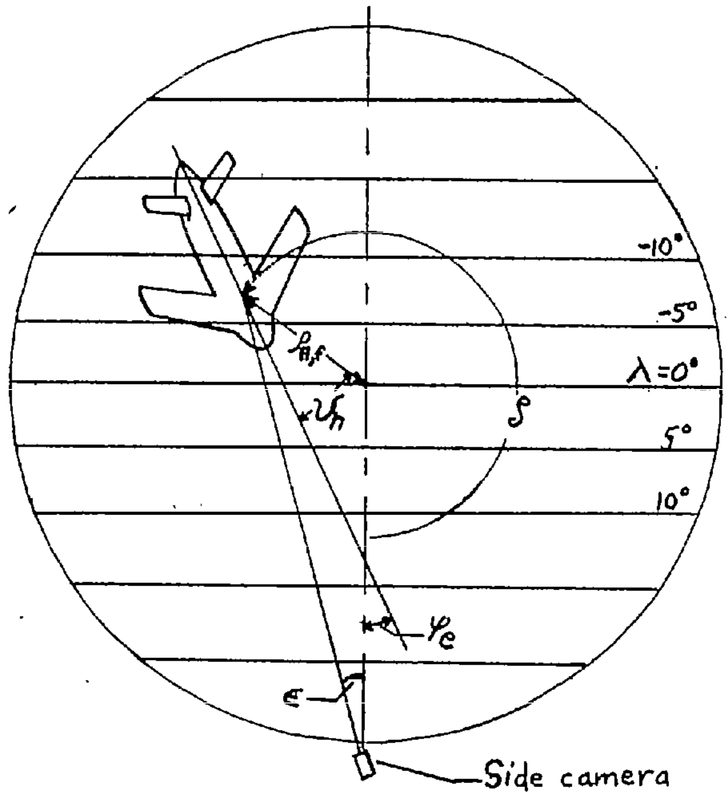

Figure 18.- Sketch illustrating model, side camera, and pertinent angles as seen from film taken by bottom camera.

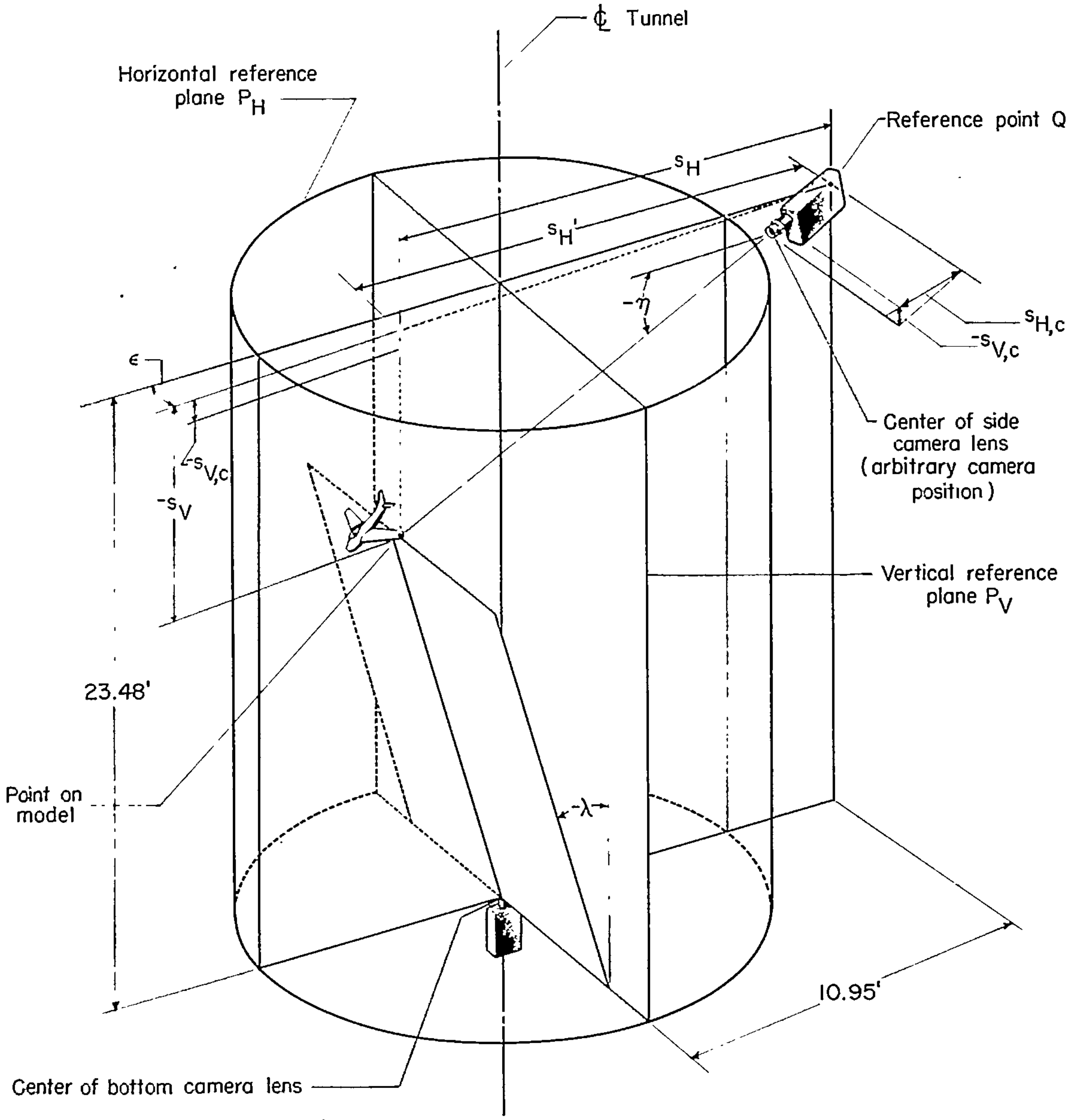

L-90539.1

Figure 19.- Sketch indicating tunnel, reference planes, angles, and distances used in determining s_V of a point on the model.

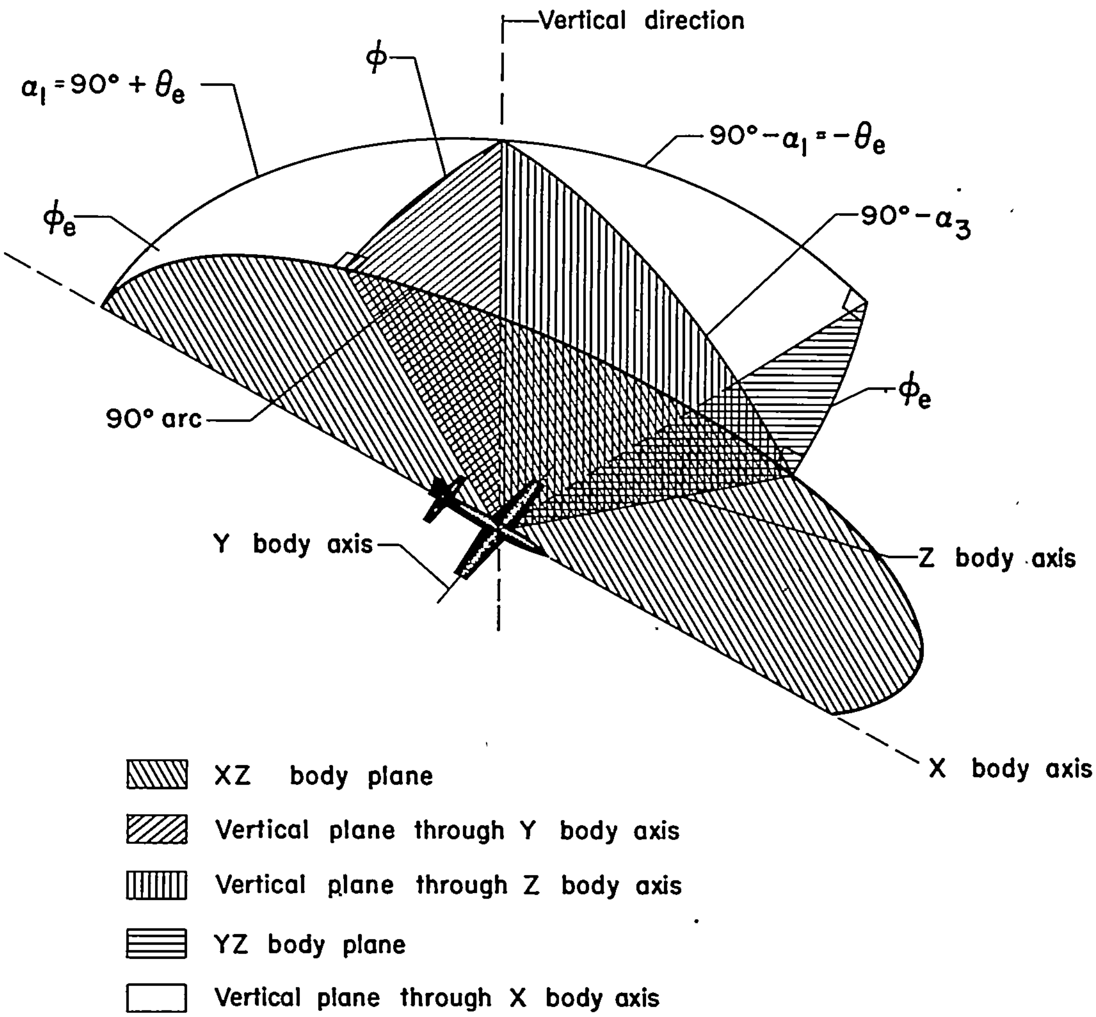

Figure 20.- Sketch showing spherical trigometric relationships between angles ϕ, θ_e, ϕ_e, and α_3. $\text{Sin } \phi_e = \frac{\sin \phi}{\cos \theta_e}$.

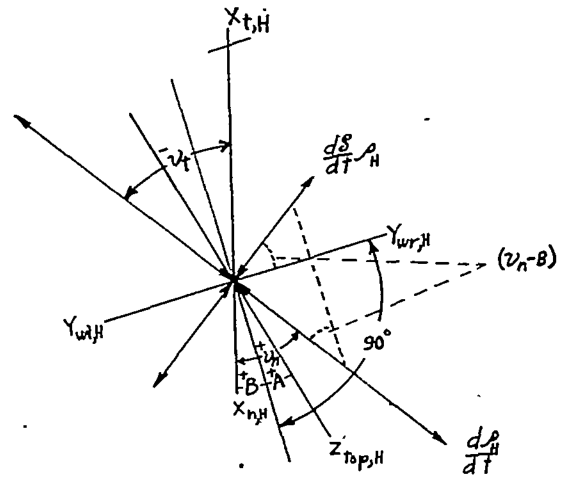

(a) ϕ positive; ν_n positive.

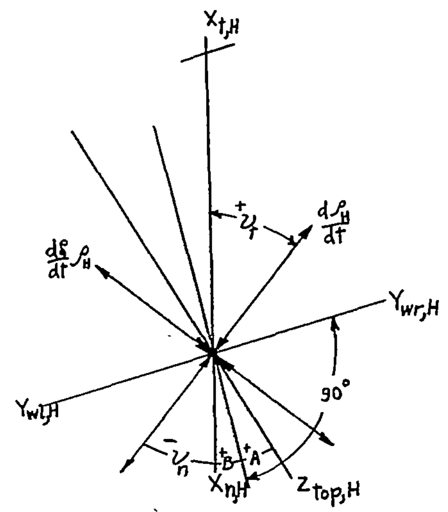

(b) ϕ positive; ν_t positive.

Figure 21.- Vector diagrams indicating various relative attitudes of possible linear velocity components in horizontal plane. Horizontal projections of body axes shown as viewed from below model, for cases (a), (b), (c), and (d). Origin of vector system is center of gravity of model. Vector direction of $\frac{d\rho_H}{dt}$ points toward various possible locations of tunnel center line, as seen on a frame of film from the bottom camera. Applicable ν selected in accordance with definition in symbols. In spin and recovery, θ_e is always negative.

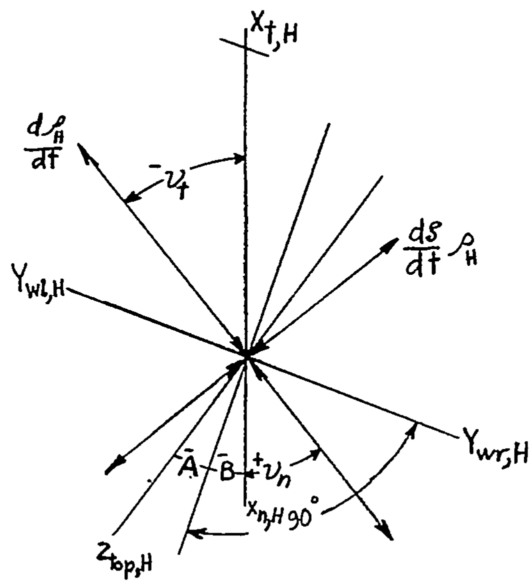

(c) ϕ negative; ν_n positive.

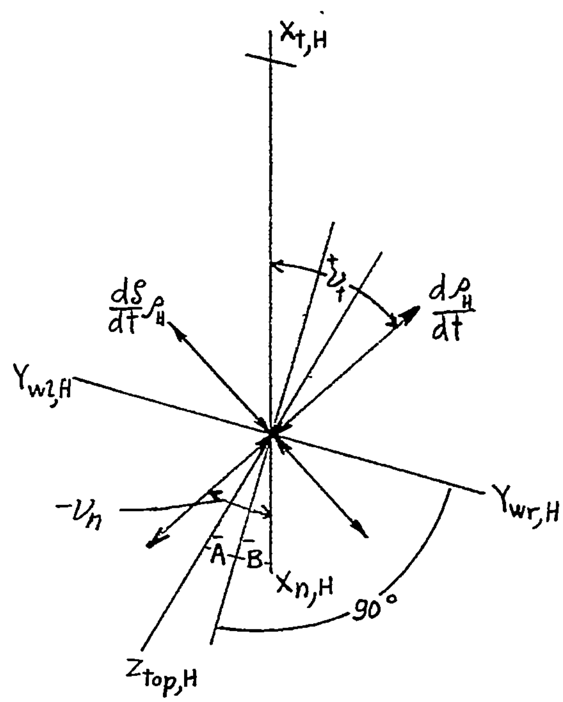

(d) ϕ negative; ν_t positive.

Figure 21.- Concluded.

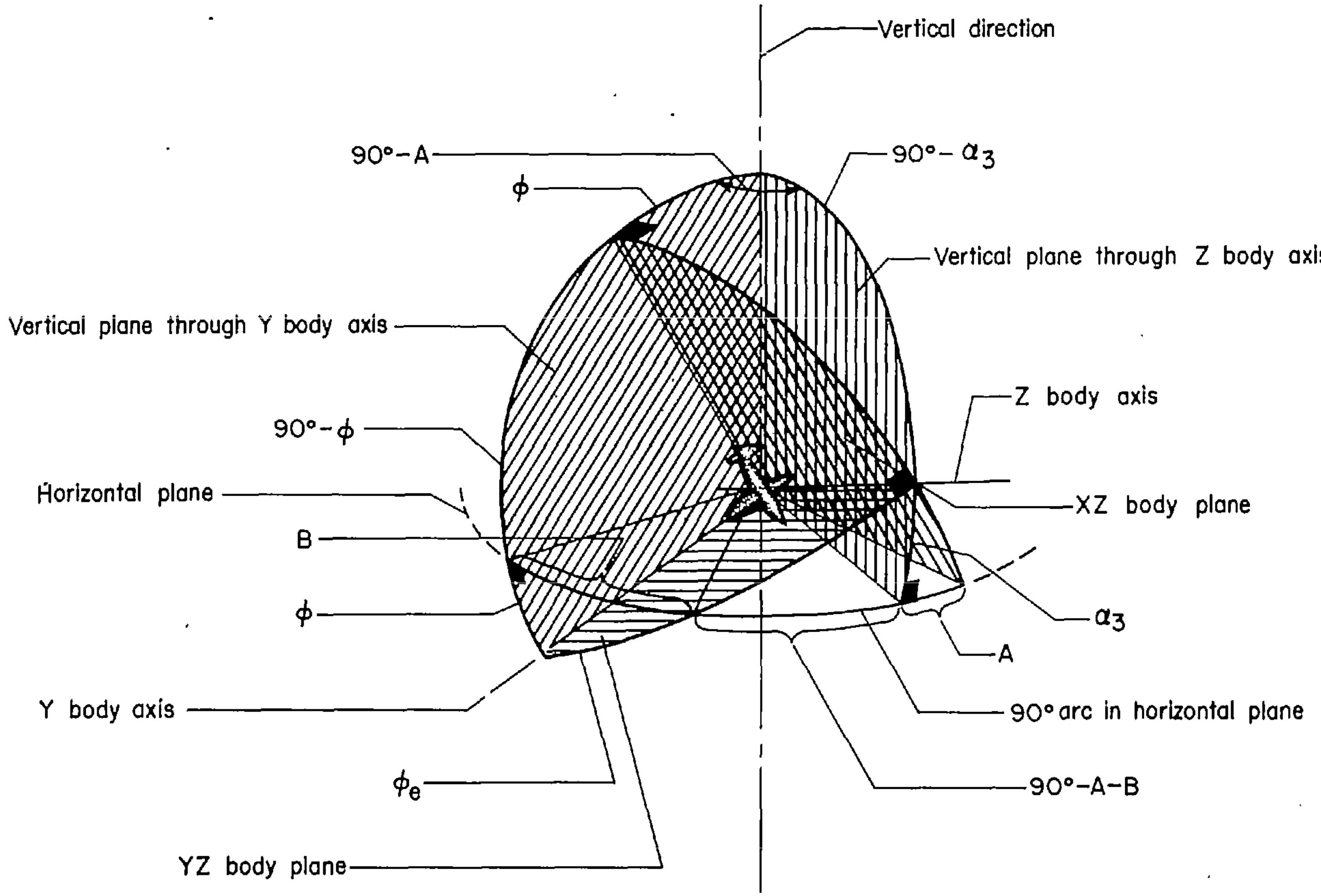

Figure 22.- Sketch indicating spherical trigonometry relationships pertinent to determination of angles A and B.

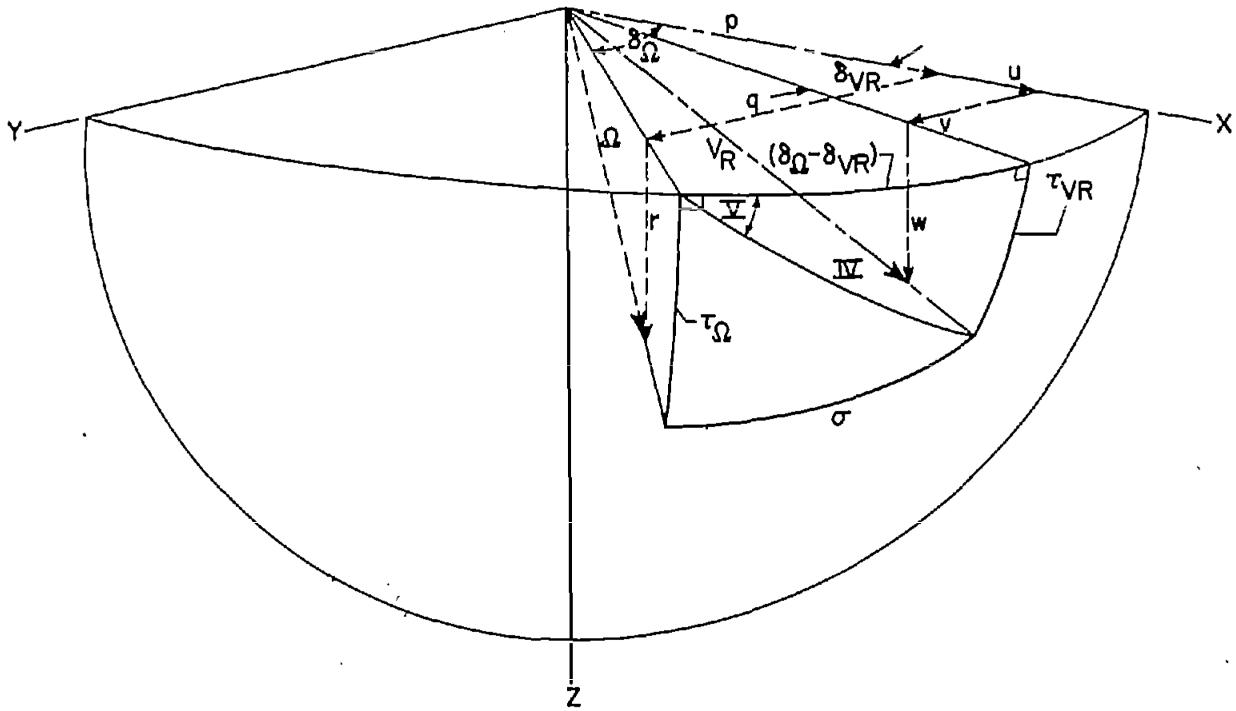

$$\cos \mathrm{IV} = \cos(\delta_\Omega - \delta_{VR}) \cos \tau_{VR}$$

$$\sin \mathrm{V} = \frac{\sin \tau_{VR}}{\sin \mathrm{IV}}$$

$$\cos \sigma = \cos \tau_\Omega \cos \mathrm{IV} + \sin \tau_\Omega \sin \mathrm{IV} \cos(90^\circ - \mathrm{V})$$

$$\cos \sigma = \cos \tau_\Omega \cos \tau_{VR} \cos(\delta_\Omega - \delta_{VR}) + \sin \tau_\Omega \frac{\sin \tau_{VR}}{\sin \mathrm{V}} \sin \mathrm{V}$$

$$\cos \sigma = \cos \tau_\Omega \cos \tau_{VR} \cos(\delta_\Omega - \delta_{VR}) + \sin \tau_\Omega \sin \tau_{VR}$$

Figure 23.- Sketch indicating vector diagrams and spherical trigonometry relationships pertinent to determination of angle σ.